Non-equilibrium dynamics in three-dimensional magnetic spin models and molecular motor-inspired one-dimensional exclusion processes

Riya Nandi

Dissertation submitted to the Faculty of the

Virginia Polytechnic Institute and State University

in partial fulfillment of the requirements for the degree of

Doctor of Philosophy

in

Physics

Uwe C. Täuber, Chair

Michel Pleimling

James Gray

Satoru Emori

March 4, 2021

Blacksburg, Virginia

Keywords: Non-equilibrium dynamics, critical dynamics, aging scaling, biological transport, molecular motors, etc.

Non-equilibrium dynamics in three-dimensional magnetic spin models and molecular motor-inspired one-dimensional exclusion processes

Riya Nandi

(ABSTRACT)

We investigate the relaxation dynamics of two distinct non-equilibrium processes: relaxation of three dimensional antiferromagnetic lattice spin models with Heisenberg interaction following a critical quench, and a one-dimensional exclusion process inspired by the gear-like motion of molecular motors.

In a system of three-dimensional Heisenberg antiferromagnets the non-conserved staggered magnetization components couple non-trivially to the conserved magnetization densities inducing fully reversible terms that enter the Langevin dynamic equation. We simulate the exact microscopic dynamics of such a system of antiferromagnets by employing a hybrid simulation algorithm that combines the reversible spin precession implemented by the fourth order Runge-Kutta integration method with the standard relaxational dynamics at finite temperatures using Monte Carlo updates. We characterize the dynamic universality class of this system by probing the early temporal window where the system exhibits aging scaling properties. We also verify an earlier renormalization group prediction that the temporal decay exponent in the two-time spin autocorrelation function exhibits *non-universality*, specifically it depends on the width of the initial spin orientation distribution. We employ a

similar numerical technique to study the critical dynamics of an anisotropic Heisenberg antiferromagnet in the presence of an external field. The phase diagram of this system exhibits two critical lines that meet at a bicritical point. We study the aging scaling dynamics for the model C critical line, probe the model F critical line by investigating the system size dependence of the characteristic spin wave frequencies near criticality, and measure the dynamic critical exponents for the order parameter including its aging scaling at the bicritical point.

We introduce a one-dimensional non-equilibrium lattice gas model representing the processive motion of dynein molecular motors over the microtubule. We study both dynamical and stationary state properties for the model consisting of hardcore particles hopping on the lattice with variable step sizes. We find that the stationary state gap-distribution exhibits striking peaks around gap sizes that are multiples of the maximum step size, for both open and periodic boundary conditions, and verify this using a mean-field calculation. For open boundary conditions, we observe intriguing damped oscillator-like distribution of particles over the lattice with a periodicity equal to the maximum step size. To characterize transient dynamics, we measure the mean square displacement that shows weak superdiffusive growth with exponent $\gamma \approx 1.34$ for periodic boundary and ballistic growth ($\gamma \approx 2$) for open boundary conditions at early times. We also study the effect of Langmuir dynamics on the density profile.

Non-equilibrium dynamics in three-dimensional magnetic spin models and molecular motor-inspired one-dimensional exclusion processes

Riya Nandi

(GENERAL AUDIENCE ABSTRACT)

Most systems found in nature are out of equilibrium. In this dissertation we investigate the relaxation dynamics of two such non-equilibrium systems:

1. We investigate a three-dimensional antiferromagnetic system relaxing towards equilibrium from an initial state that is driven far away from equilibrium at the point in the parameter space where the system undergoes a second-order phase transition. We devise a novel simulation method that captures emerging dynamic universal features, and scaling features at these points of continuous phase transition in the early times of relaxation when the system is still far away from equilibrium.

2. Cytoplasmic dyneins are one of three kinds of motor proteins that move on tubular structures called microtubules carrying and transporting cellular cargo inside the cells. Unlike the other molecular motors that move forward with fixed step sizes, the dyneins have been experimentally observed to vary their step size depending on the amount of cargo they are carrying. We model an exclusion process in a one-dimensional lattice inspired by the motion of the dynein molecular motors where the motors can hop from one to four steps depending on their internal states. We study the effect of this variable step size on the dynamics of a collection of dyneins. We observe intriguing oscillating density profiles and discrete peaks in the distribution of

empty sites. Our results suggest self-organization among the motors and the empty sites.

Dedication

I dedicate this work to my beloved parents whose unfaltering love and encouragement makes every dream seem achievable

Acknowledgments

I would like to acknowledge the tremendous contribution of my advisor Dr. Uwe C. Täuber in the accomplishments of my graduate career. His guidance, constructive criticisms, and unyielding faith in me motivated me to work harder to become a better researcher. Discussions with him on and beyond research topics have always been thoroughly enjoyable and educational. I hope to continue to learn from him for a long time in the future.

I would like to thank Dr. Michel Pleimling for his scientific advice through many fruitful discussions during my PhD. I also want to thank my other committee members Dr. Satoru Emori and Dr. James Gray for their valuable suggestions and advice during the course of my graduate career.

I wish to acknowledge Dr. Priyanka for her scientific guidance during our collaborations and for her friendship and support beyond research. Additionally, I would like to thank the past and current members of our research group: Dr. Harshwardhan Chaturvedi, Dr. Sheng Chen, Dr. Ruslan Mukhamadiarov, Dr. Shannon Serrao, Dr. Shengfeng Deng and Hong Yao for their counsel and feedback on my research over the course of the last six years. I have enjoyed and learned a lot from the engaging discussions on our various research fields that we had in Robeson, 306 and over Zoom this past year! I thank our graduate program coordinator, Betty Wilkins, our program support technician, Katrina Loan, and our IT staff members Roger Link and Travis Heath for their kind help whenever needed.

My graduate school journey and my time in Blacksburg would not have been half as enjoyable if not for the company of the amazing friends I made here! I wish to especially mention Rathsara Herath, Amrita Chakraborty, Arian Vezvaee and Dr. Madhurima Nath; thank you for helping me navigate through the fundamentals of grad life! I am really fortunate and most thankful for the friendships of the following women across the various junctures of my life; Sayani Ghosh, Pallabi Das, Dr. Shamreen Iram, Dr. Shinibali Bhattacharyya, Dr. Sucheta Majumdar, Henna Popli and Shohini Bhattacharya. You all are incredibly talented and have been a continued source of inspiration in my life.

I want to express my most sincere gratitude to my family; my parents Rekha Nandi and Mohit Kumar Nandi and my sister Mahua Nandi to whom I give all the credit for who I am today and who gives me strength and purpose to fulfil my dreams everyday. Finally, I want to thank my husband Adbhut Gupta for his wholehearted love and support through these last five years, for supporting my choices, for being my PhD partner and for always believing!

The research was sponsored by the U.S. Army Research Office and was accomplished under Grant Number W911NF-17-1-0156.

Contents

List of Figures

List of Tables

Chapter 1

Introduction

Thermodynamic equilibrium is a state of a system which is perfectly at balance with its surrounding, i.e, there is no net flow of matter or energy either between the system and its surrounding or within the system. From the *second law of thermodynamics*, it is well-known that the equilibrium state of a system corresponds to the one that has the highest amount of unpredictability or the highest number of microstates Ω. In other words, the equilibrium state maximizes the *entropy* of the system, where entropy is defined as,

$$S = k_B \ln \Omega.$$

Thus, the probability of finding a system in equilibrium manifestly depends on the number of microstates: $P_r(E) \propto \Omega$. Utilizing thermodynamic relations between energy, entropy, and temperature, one arrives at the stationary Boltzmann probability distribution for equilibrium states:

$$P_r(E) = \frac{1}{Z} \exp(-\beta E) \ , \tag{1.1}$$

where $\beta = \frac{\partial \ln \Omega(N,V,E)}{\partial E}$ is related to the inverse of temperature in a canonical ensemble with the system surrounded by a heat bath, E is the total energy of the system's state, and Z is the partition function. Most physical and biological systems prevalent in nature are, however, out-of-equilibrium, i.e, they are evolving, either relaxing towards the state of equilibrium or are driven out of equilibrium at all times via a steady influx of energy and/or matter from their surrounding environment. As stated by Erwin Schrödinger in his book *What is Life?* [1], all living beings remain alive precisely by staying out of equilibrium: "How does the living organism avoid decay? The obvious answer is: By eating, drinking, breathing, and (in the case of plants) assimilating." The dynamics of living cells where organelles and proteins are exchanged between the cell and the surrounding environment continually through the membranes; chemical reaction kinetics; spread of epidemics; financial models of the stock market, and flocking dynamics of insects and animals are some of the paradigmatic examples of non-equilibrium processes.

While equilibrium thermodynamics is characterized by time-independent state variables such as temperature, pressure, or chemical potential, non-equilibrium thermodynamics can describe the continuous-time evolution of systems subject to net non-zero forces. The dynamic properties of a non-equilibrium process are characterized by transport coefficients and relaxation rates. Another essential distinction between the two processes is through the manifestation of *detailed balance* [2]: Let us consider a discrete set of states of a system $i, j = 1, 2, ...,$ $P[i]$ be the probability of finding the system in state i, and the transition rate from state i to j denoted by k_{ij}. The condition of detailed balance necessary for equilibrium requires

$$\text{flux from i to j} = P[i]k_{ij} = P[j]k_{ji} = \text{flux from j to i}$$

for every pair of states i, j. The constant input of matter and energy from the surroundings ensures that this condition is violated in non-equilibrium processes. Thus, non-equilibrium processes are characterized by non-zero probability currents flowing through the system. However, certain non-equilibrium systems evolve towards time-invariant stationary states called non-equilibrium steady states (NESS) which satisfy

$$\text{net flow into i} = \sum_{j \neq i} P[j]k_{ji} = \sum_{i \neq j} P[i]k_{ij} = \text{net flow out of i.}$$

In this dissertation, we study two different types of non-equilibrium phenomena: One is the theory of critical phase transition dynamics in a three-dimensional system of magnetic spins where the system is driven far from equilibrium and we study the dynamics of its relaxation towards equilibrium; the other is a one-dimensional asymmetric exclusion model inspired by the motion of dynein motor proteins that perform hydrolysis-driven hops, which after an initial transient dynamics period settles into a non-equilibrium steady state.

The dissertation is organized into two parts: In the first part, we discuss the non-equilibrium dynamics in three-dimensional antiferromagnets starting with a brief literature review of critical dynamics. In the second part, we introduce the asymmetric simple exclusion processes (ASEP) in the context of biological transport and discuss our model and its stationary state and transient dynamics results in the subsequent chapter.

Chapter 2

Dynamic critical phenomena

Physical systems near a continuous phase transition point develop long-range correlations that extend much beyond the microscopic length and time scales. Such points in the parameter space, known as *critical points*, exhibit rich and interesting physical properties (for overviews, see, e.g, Refs. [3, 4, 5, 6, 7, 8, 9, 10, 11]). Critical points are often associated with symmetry breaking as they separate an ordered phase from a disordered one, and the quantity that gains a finite non-zero value as one crosses the point is known as the *order parameter*. The order parameter dynamics at this point of transition is dominated by large fluctuations, which in turn results in correlations that extend to the size of the system, and thus the order parameter relaxes slowly towards its equilibrium value. Singularities originating due to the diverging correlation length ξ are expressed in terms of power-law decays as a function of the distance from the critical point,

$$\xi \sim |\tau|^{-\nu}, \ \tau = T - T_c \ , \tag{2.1}$$

where T_c is the critical temperature and ν is a *universal critical exponent*. Thus, the growing spatio-temporal correlations among the interacting individual particles in the system leads to the emergence of universal features that are independent of the microscopic details of the system as one approaches the asymptotic limit. As a consequence of the growing correlations, the system exhibits scale-invariance, i.e, they behave similarly at all length and time scales. This is the fundamental essence of *universality* wherein systems with diverse microscopic properties can be grouped under the same universality class if their order parameter correlation divergences can be characterized by the same asymptotic exponents. The scale-invariant limit of systems near a critical point is the basis upon which renormalization group (RG) theory is used as the standard mathematical approach to investigate the theory of critical dynamics. In the RG treatment, one approaches the "fixed points" where the system becomes invariant under scale transformations which is equivalent to approaching the singularities near a critical point described by universal exponents.

2.1 Landau's phenomenological theory

To formulate a general framework for second-order phase transitions, Landau developed a phenomenological approach by proposing the expansion of the free energy of the system in powers of the mean-field order parameter ϕ (since close to the critical point $\phi << 1$) while respecting the symmetries of the Hamiltonian [11, 12, 13]. Thus, for a Hamiltonian with $(\phi \leftrightarrow -\phi)$ symmetry, one can write,

$$f(\phi) = r(\tau)\phi^2 + u\phi^4 + ... \tag{2.2}$$

where $\tau = \frac{T-T_c}{T_c} << 1$ and $r(\tau)$ $(\propto \tau)$ is a temperature dependent prefactor. One can then minimize $f(\phi)$ to obtain the equilibrium value of ϕ,

$$f'(\phi) = 0 \Rightarrow \phi = 0, \pm\sqrt{\frac{-r(\tau)}{2u}}.$$

Thus, for $r(\tau) > 0$ or temperatures $T > T_c$, there is only one real solution $\phi = 0$. Critical phase transition is determined by the condition $r(\tau) < 0$ which spontaneously breaks the symmetry in the system and forces the order parameter value to settle in one of the two minimas $+r/2u$ or $-r/2u$. One can now obtain the mean-field *critical exponents* characterizing the power laws for static quantities such as the order parameter and the specific heat near critical point:

$$\phi \propto |\tau|^{\beta}, \qquad \beta = 1/2 \tag{2.3}$$

$$C_h = -\left(\frac{\partial^2 f}{\partial \tau^2}\right) \propto \begin{cases} |\tau|^{-\alpha}, & \tau < 0, \\ 0, & \tau > 0 \end{cases} \qquad \alpha = 1 \tag{2.4}$$

Adding the lowest-order symmetry-breaking field term H_{ext} to the free energy and ignoring higher order terms one obtains,

$$f(\phi) = r(\tau)\phi^2 + u\phi^4 - H_{ext}\phi$$

The equilibrium value of ϕ is now given by the equation

$$2r\phi + 4u\phi^3 = H_{ext}.$$

Hence, the order parameter susceptibility diverges as,

$$\chi_T = \left(\frac{\partial H_{ext}}{\partial \phi}\right)^{-1} \propto |\tau|^{-\gamma}, \qquad \gamma = 1. \tag{2.5}$$

Finally, setting $\tau = 0$ one obtains the critical isotherm,

$$\phi \propto H_{ext}^{1/\delta}, \qquad \delta = 3. \tag{2.6}$$

In the context of the mean-field treatment, another important relation is the *fluctuation-response theorem* that relates the order parameter correlation function to the local response,

$$\chi_{ij} = \frac{1}{k_B T} C_{ij} \ , \tag{2.7}$$

where $C_{ij} = \langle \sigma_i \sigma_j \rangle - \langle \sigma_i \rangle \langle \sigma_j \rangle$ is the two-point spin correlation function for a magnetic system and χ_{ij} becomes the thermodynamic susceptibility χ_T when integrated over the entire system in the continuum limit.

2.2 Scaling Hypothesis

Landau's phenomenological theory demonstrates the striking fact that quite distinct continuous phase transitions driven by entirely different microscopic mechanisms are characterized by identical static critical exponents α, β, γ, and δ. Thus, systems may be classified into *static universality classes* described by the same critical exponents, that, for short-range microscopic interactions, depend only on the underlying symmetry of the order parameter and the system's dimensionality. The scaling hypothesis emerged as a generalization to the Landau theory where one assumes that in the vicinity of the phase transition, the free energy and the order parameter correlations become generalized homogeneous functions of the distance from the critical point [11, 14]. The scaling ansatz for the free energy states,

$$f(\tau, H_{ext}) = |\tau|^{(2-\alpha)} f_{\pm}(H_{ext}/|\tau|^{\Delta}) \tag{2.8}$$

where $f_{\pm}(x)$ are the scaling functions above and below the critical point, and α and Δ are the scaling exponents. From Eqn. (2.8), relations between the different critical exponents are obtained and it appears that only *two independent critical exponents* are sufficient to describe the transition.

In a similar spirit, one writes down the scaling ansatz for the order parameter correlation function in momentum space,

$$C(\tau, q) = |q|^{-2+\eta} C_{\pm}(q\xi) \tag{2.9}$$

with *correlation length* ξ diverging at T_c as,

$$\xi \propto |\tau|^{-\nu}.$$

A non-zero value of *Fisher exponent* η denotes the fractal nature of the spatial correlations near T_c.

As larger regions of the system become correlated, the relevant time scales of dynamic processes also increase. This leads to the generalization of the static scaling hypothesis to dynamic scaling. The characteristic relaxation time scale diverges as a function of the correlation length,

$$t_c \sim \xi^z \sim |\tau|^{-z\nu} \ , \tag{2.10}$$

where z is the dynamic critical exponent that gives the measure of the *critical slowing down* near T_c. The dynamic correlation function thus takes the form,

$$\begin{aligned} C(\tau, q, \omega) &= \frac{2\pi}{\omega} f\Big(\frac{\omega}{\omega_c(\tau, q)}\Big) C(\tau, q) \ , \\ &= |q|^{-z-2+\eta} C_{\pm}\Big(q\xi, \frac{\omega}{\omega_c}\Big) \ , \end{aligned} \tag{2.11}$$

and the characteristic frequency scales as $\omega_c \sim |q|^z \omega_{\pm}(q\xi)$.

2.3 Langevin Description

The presence of these singularities described in the previous section indicate that the order parameter dynamics is driven by large fluctuations which the mean-field treatment of Landau theory completely ignores. Yet beyond the upper critical dimension d_c, the d dependence disappears, and the critical exponents may be obtained by employing straightforward mean-field approximations; for $d < d_c$, critical fluctuations dominate and cause marked deviations from mean-field predictions. A correct formulation, thus, must include these critical fluctuations and the associated spatial correlations. Consequently, one can write down the Landau-Ginzburg-Wilson Hamil-

tonian that expresses the free energy as a functional of the coarse-grained spatially inhomogeneous order parameter density:

$$\mathcal{H}[\phi(\mathbf{x})] = \int d^d x \Big(r\phi(\mathbf{x})^2 + u\phi(\mathbf{x})^4 + c(\nabla\phi(\mathbf{x}))^2 - h(\mathbf{x})\phi(\mathbf{x}) \Big) \tag{2.12}$$

One can then obtain the correct fixed points and the static exponents for the given model by applying RG techniques. However, physical systems that in thermal equilibrium fall into the same static universality class may still display distinct dynamical critical scaling behavior owing to different dynamics of relaxation times: Crucial differences arise if the order parameter is conserved under the dynamics or not; and if it is coupled statically or dynamically to other conserved slow modes [4, 6, 7, 8, 9, 11]. A classification of the different dynamic universality classes describing the equilibrium transitions named models A-J was given by Halperin and Hohenberg in their paradigmatic 1977 review article [4].

For the simple case of a non-conserved order parameter, the critical dynamics is described by a stochastic Langevin equation,

$$\frac{\partial\phi(\mathbf{x},t)}{\partial t} = -D\frac{\delta\mathcal{H}(\phi)}{\delta\phi} + \eta(\mathbf{x},t) \tag{2.13}$$

where D denotes a constant relaxation rate and η is a Gaussian stochastic force. In order to ensure that at long times the system relaxes to the equilibrium distribution with the appropriate Boltzmann weights $P_{st}(\phi) = \frac{1}{Z}e^{-\mathcal{H}(\phi)/k_BT}$, the Einstein relation must be satisfied:

$$\langle\eta(\mathbf{x},t)\rangle = 0;\ \langle\eta(\mathbf{x},t)\eta(\mathbf{x}',t')\rangle = 2Dk_BT\delta(\mathbf{x}-\mathbf{x}')\delta(t-t') \tag{2.14}$$

This describes the critical dynamics of *model A*. However, if the order parameter is a conserved quantity, the order parameter density must satisfy a continuity equation. Hence the diffusion coefficient D is replaced by the operator $D\nabla^2$ in both Eqn. 2.13 and 2.14. This constitutes *model B*. If the order parameter density couples nonlinearly to a conserved mode, one must also include reversible mode-coupling terms in the above dynamical equations [4, 9, 15]. The following chapters will be focused on examples of this later scenario.

2.4 Aging scaling

When a stochastic system is prepared in a random initial state of very small correlations and then quenched suddenly to its critical parameters, the system is driven far away from equilibrium and the order parameter is forced to relax to equilibrium with slow dynamics dominated by critical fluctuations. In the very early stages of such relaxation, at microscopic times $t \sim t_{mic}$, the dynamics is governed by microscopic details of the system and is thus, non-universal. On the other hand, the critical scaling behavior introduced in the previous sections implicitly assumed the long-time asymptotic limit where the system was not affected by its initial state of preparation. However, an intermediate timescale was observed and reported by Janssen, Schaub, and Schmittmann in 1969 that sets in after the microscopic time scale and eventually crosses over to the long-time behavior [16]. This new regime, named the "critical initial slip", also exhibits universal features characterized by a new critical exponent that may or may not be independent of the long-time exponents. The time-scale of this relaxation regime is set by the initial values of the order parameter and the correlations at which the system was prepared. Thus, during this stage of the non-equilibrium relaxation, the system retains the memory of its initial state of preparation for a time scale s, t that extends beyond the microscopic time scales t_{mic} to the range of its relaxation time scale t_{rel}: $t_{mic} << s, t < t_{rel}$. This causes the system to break time-translational invariance, and any two-time observable, such as the two-time order parameter correlation function, depends on both the waiting and observation times s and t, respectively. For purely diffusive relaxation of model A, one can write down the two-time correlation function at $T = T_c$ as,

$$C(q,t,s) = |q|^{-2+\eta}\left(\frac{t}{s}\right)^{\theta-1} C_{\pm}(q\xi, q^z t) \tag{2.15}$$

and the order parameter can be written as,

$$M(t) = M(0)t^{\theta'} f_M\left(t^{\theta'+\beta/\nu z} M(0)\right) . \tag{2.16}$$

Here $\theta' = \theta + (2 - z - \nu)$ and θ is known as the *initial slip exponent* and

$$f_M(x) = \begin{cases} 1, \ x \sim 0 \\ 1/x, \ x \to \infty \end{cases} \tag{2.17}$$

In situations where the relaxation of the system is governed by only one time-dependent length scale, such as in the critical dynamics of magnetic systems, one can write down a general expression for the autocorrelation functions [17],

$$C(s,t) = s^{-b} f(t/s) \ . \tag{2.18}$$

For long times ($t >> s$), the scaling function follows a simple power-law $f(t/s) \propto (t/s)^{-\lambda/z}$. Such a system exhibiting slow algebraic relaxation, broken time-translational invariance, and satisfying dynamic scaling is said to be undergoing *physical aging* [17]. Thus, from the early time scaling of the autocorrelation function and the order parameter, Eqns. (2.15) and (2.16), the dynamic exponent z governing the long-time stationary scaling behavior becomes accessible much earlier in the relaxation process, and one can easily avoid the hindrance caused by the critical slowing-down. This renders the aging-scaling relaxation with critical parameters an efficient way to numerically characterize the dynamic universal properties of such systems [15]. In the following chapters, we employ this method for our study of different dynamic universality classes.

2.5 Structure of part I

The following chapters are structured as follows: In chapter 3, we investigate the non-universal critical relaxation dynamics of three-dimensional isotropic antiferromagnets using a novel hybrid algorithm combining the deterministic fourth-order Runge-Kutta integration scheme and stochastic Monte Carlo updates. In chapter 4, using similar computational tools, we characterize the two critical lines and a bi-critical point present in the phase space of a three-dimensional anisotropic antiferromagnet in the presence of an external field. A comprehensive conclusion to the dissertation is provided in chapter 7, which includes a summary of the above-mentioned chapters on the critical dynamics and provides an outlook to the possible future directions to this research.

Chapter 3

Non-universal critical aging-scaling of isotropic antiferromagnet

This chapter is adapted with minor changes from our publication [18]
Riya Nandi and Uwe C. Täuber, "Nonuniversal critical aging scaling in three-dimensional Heisenberg antiferromagnets", Phys. Rev. B (2019) 99, 064417, "Copyright (2019) by the American Physical Society."

My contributions to this publication include developing the simulation algorithm for exploring the aging-scaling dynamics in three-dimensional antiferromagnets, analysing the obtained data, and preparing the first draft of the manuscript including the figures.

3.1 Introduction

Physical systems near the critical point display characteristic singularities in their thermodynamic properties as well as transport coefficients that originate from the systems' diverging correlation length. As the governing collective length and time scales diverge at the critical point, systems with infinitely many degrees of freedom acquire scale invariance as an emergent new symmetry, which is reflected in non-trivial scaling laws for physical observables that mathematically assume the form of generalized homogeneous functions. Yet in a finite system, say with sufficiently large linear extension L, the characteristic relaxation time should follow the finite-size scaling law $t_c(\tau, L) = \xi(\tau)^z\, \hat{t}(\xi/L)$, with $\hat{t}(0) = \text{const.}$, while the scaling function at large arguments $\hat{t}(y \gg 1) \sim y^{-z}$ in order to eliminate the τ dependence as $\tau \to 0$, implying $t_c(0, L) \sim L^z$, the *dynamic exponent* z defining the dynamic universality class of the system.

Despite the split of static into varied dynamic universality classes, quite distinct physical systems may be described by the same dynamical critical exponent; e.g., this is

the case for planar ferromagnets (model E in Hohenberg and Halperin's classification scheme [4]), superfluid Helium 4 (model F), and isotropic antiferromagnets (model G), for which $z = d/2$ in $d \leq d_c = 4$ spatial dimensions [19, 20, 21]. Indeed, these systems may be subsumed into one $O(n)$-symmetric dynamical universality class in which an n-component non-conserved order parameter ($n = 2$ for models E and F, $n = 3$ for model G) is reversibly coupled to $n(n-1)/2$ non-critical conserved fields (i.e., a scalar for model E, a three-component vector field for model G) [22, 23, 24].

A thorough theoretical understanding and a systematic classification of dynamical systems near criticality have been gained through extensive numerical simulations [25, 26], and by means of the dynamic renormalization group approach which crucially exploits the emerging scale invariance [3, 4], especially its field-theoretic variant [5, 7, 8, 9, 10, 11]. This extends beyond the steady-state kinetics to the critical non-equilibrium relaxation regime; here, the system is initially prepared in a disordered configuration with prescribed (usually Gaussian) probability distribution, and is subsequently quenched to the critical point, i.e., forced to evolve under critical parameter values. Hence it can only relax to stationarity algebraically slowly and retains memory to the initial state, resulting in the breaking of time translation invariance and associated characteristic aging scaling behavior for the spatial two-time order parameter correlation function

$$C(t, s, r, \tau) = r^{-(d-2+\eta)}\,(t/s)^{\theta-1}\;\hat{C}(r/\xi, t/\xi^z) \tag{3.1}$$

in the limit $t \gg s$, with the standard static Fisher exponent η and the initial-slip exponent θ [11, 16, 17, 27, 28]. For the autocorrelations ($r = 0$) at criticality ($\tau = 0$), this turns into a simple aging scaling form

$$C(t, s) \sim s^{-b}\,(t/s)^{-\lambda/z} \tag{3.2}$$

with the aging collapse exponent $b = (d-2+\eta)/z$ and the autocorrelation exponent $\lambda = d - 2 + \eta + z(1-\theta)$. Importantly, therefore, the dynamic exponent z can be directly inferred from the early-time relaxation scaling; one thus need not necessarily contend with the long relaxation times to reach the quasi-stationary regime.

For $O(n)$-symmetric systems with conserved order parameter, $\lambda = d+2$ exactly [29], implying the exact scaling relation $\theta = 1-(4-\eta)/z$. For purely irreversible diffusive relaxation (model B) with $z = 4-\eta$, consequently $\theta = 0$ [16]; and similarly for isotropic ferromagnets (model J) whose dynamics entails a reversible spin precession term, $z = (d+2-\eta)/2$ for $d \leq 6$, whence $\theta = -(6-d-\eta)/(d+2-\eta) < 0$ [30]. In contrast, if the order parameter is not conserved, θ in general represents

an independent critical exponent. It assumes a universal value for purely dissipative relaxational kinetics (model A) that can for instance be computed perturbationally in a dimensional $\epsilon = d_c - d$ expansion; to first order $\theta = (n+2)\,\epsilon/4(n+8) + O(\epsilon^2)$ for $d \leq d_c = 4$ [16, 27].

Yet in their one-loop renormalization group analysis for the critical dynamics of a non-conserved order parameter that is subject to reversible mode coupling to a non-critical conserved field, based on a continuum description in terms of coupled non-linear Langevin equations [11, 23, 24], Oerding and Janssen found in 1993 that the initial-slip exponent θ explicitly depends on the Gaussian distribution width c_0 for the magnitudes of the initial values of the conserved mode; quite surprisingly therefore, they predicted non-universal critical aging scaling for this universality class [30]. Indeed, in their analysis, $z\,\theta = -\gamma_\lambda - \eta_0/2$ is determined by the anomalous scaling dimension of the order parameter relaxation rate $\gamma_\lambda = \epsilon/2$ (which holds to all orders at the strong dynamic scaling fixed point) and of the fields on the initial-time surface $\eta_0 = (3c_0/2 - 16/11)\,\epsilon + O(\epsilon^2)$ (for $n = 3$), which increases linearly with the width c_0. To our knowledge, this striking prediction had not yet been tested either numerically or experimentally before.

In this chapter, we provide numerical evidence, gathered through a hybrid simulation algorithm for the critical dynamics of isotropic antiferromagnets on a three-dimensional lattice which combines reversible spin precession with relaxational Kawasaki spin exchange processes, that lends support to this remarkable assertion: We demonstrate that the spin autocorrelation exponent λ depends on the width of the initial spin orientation distribution, whereas we measure a universal value b for the aging scaling exponent.

3.2 Model and simulation algorithm

We consider the isotropic Heisenberg model (in the absence of an external field) with the Hamiltonian

$$\mathcal{H} = -J \sum_{<ij>} \vec{S}_i \cdot \vec{S}_j \tag{3.3}$$

governing the nearest-neighbor exchange interactions of three-component vector spin variables $\vec{S}_i$ on a three-dimensional simple cubic lattice of linear size L (with L up to 70 lattice sites) with with periodic boundary conditions. For both ferro- ($J > 0$) and antiferromagnetic ($J < 0$) exchange couplings, a continuous transition from a disor-

dered high-temperature paramagnetic state to the ordered phase occurs for $L \to \infty$ at $k_{\mathrm{B}}T_c^{\infty} \approx 1.446\,|J|$ in three dimensions, which belongs to the static universality class of the $O(3)$-symmetric Ginzburg–Landau–Wilson vector model with Fisher exponent $\eta \approx 0.0355$ [31]. For classical Heisenberg magnets, this has been confirmed extensively through high-resolution Monte Carlo simulations [32, 33]. Sophisticated methods such as single-cluster updates and histogram reweighing, optimization techniques, and finite-size scaling have provided very accurate estimates of the static critical exponents [33, 34].

In the absence of an external field, the Hamiltonian (3.3) is rotationally symmetric in spin space, and hence the components of the total magnetization $M^\alpha = \sum_i S_i^\alpha$ ($\alpha = x, y, z$) are conserved under the dynamics: $\{\mathcal{H}, M^\alpha\} = 0$; here we employ a classical notation in terms of Poisson brackets, following the standard correspondence with quantum-mechanical commutators. For an antiferromagnet ($J < 0$), the order parameter is however represented by the components of the non-conserved staggered magnetization vector ϕ^α, with alternating ± 1 signs affixed to adjacent lattice sites.

3.2.1 Mesoscopic Langevin Dynamics

Upon coarse-graining, the microscopic quantum spin variables S_i^α are substituted by classical mesoscopic fields $S^\alpha(\vec{x})$ and the Hamiltonian by an effective free energy functional $\mathcal{H}[S]$. The reversible dynamics at $T = 0$ is fully determined by the Poisson brackets $Q^{\alpha\beta}(\vec{x}, \vec{x}') = \{S^\alpha(\vec{x}), S^\beta(\vec{x}')\} = g \sum_\gamma \epsilon^{\alpha\beta\gamma}\, S^\gamma(\vec{x})\, \delta(\vec{x} - \vec{x}')$ with a dimensionful mode-coupling constant g that originates from taking the continuum limit. At finite temperatures, a hydrodynamic analysis [35] or the Mori–Zwanzig projector formalism (see, e.g., Ref. [36]) leads to Langevin-type stochastic partial differential equations

$$\frac{\partial S^\alpha(\vec{x}, t)}{\partial t} = F^\alpha_{\mathrm{rev}}[S](\vec{x}, t) + F^\alpha_{\mathrm{rel}}[S](\vec{x}, t) + \zeta^\alpha(\vec{x}, t) \tag{3.4}$$

for the fields $S^\alpha(\vec{x})$ with the general reversible forcing

$$F^\alpha_{\mathrm{rev}}[S] = -\int d^d x' \sum_\beta \left[Q^{\alpha\beta}\, \frac{\delta \mathcal{H}[S]}{\delta S^\beta(\vec{x}')} - k_B T\, \frac{\delta Q^{\alpha\beta}}{\delta S^\beta(\vec{x}')} \right], \tag{3.5}$$

which satisfies the general equilibrium condition that the associated probability current be divergence-free in the dynamical variable space [11, 37]. The stochastic forcing may be taken to be Gaussian white noise ζ^α with vanishing mean $\langle \zeta^\alpha \rangle = 0$

and correlator

$$\langle \zeta^\alpha(\vec{x},t)\,\zeta^\beta(\vec{x}',t')\rangle = 2\lambda\, k_{\rm B}T\,(i\nabla)^a\,\delta(\vec{x}-\vec{x}')\delta(t-t')\delta^{\alpha\beta}\ , \tag{3.6}$$

whose strength obeys Einstein's relation with the corresponding relaxation constant λ; here $a = 0$ for dissipative, non-conserved fields, whereas $a = 2$ for diffusive conserved fields, such that the irreversible relaxation term towards a minimum of the free energy $\mathcal{H}[S]$ becomes

$$F^\alpha_{\rm rel}[S] = -\lambda\,(i\nabla)^a\,\frac{\delta\mathcal{H}[S]}{\delta S^\alpha}\ . \tag{3.7}$$

For the $O(3)$-symmetric Heisenberg spin system, the second, finite-temperature term in $F^\alpha_{\rm rev}[S]$ vanishes. For isotropic ferromagnets ($J > 0$) with conserved magnetization order parameter, one then immediately obtains the model J Langevin equation [4, 35, 37]

$$\frac{\partial\vec{S}(\vec{x},t)}{\partial t} = g\,\vec{S}(\vec{x},t)\times\frac{\delta\mathcal{H}[\vec{S}]}{\delta\vec{S}(\vec{x},t)} + \lambda\,\nabla^2\,\frac{\delta\mathcal{H}[\vec{S}]}{\delta\vec{S}(\vec{x},t)} + \vec{\zeta}(\vec{x},t)\ . \tag{3.8}$$

For isotropic antiferromagnets ($J < 0$), one must consider the Poisson brackets between the components of the non-conserved staggered magnetization order parameter ϕ^α and the non-critcal conserved magnetization fields S^α. Yet it turns out that the mode-coupling constant $\tilde{g}$ in the Poisson bracket $\{\phi^\alpha(\vec{x}),\phi^\beta(\vec{x}')\} = \tilde{g}\sum_\gamma \epsilon^{\alpha\beta\gamma}\,S^\gamma(\vec{x})\,\delta(\vec{x}-\vec{x}')$ is irrelevant in the renormalization group sense. With $\{\phi^\alpha(\vec{x}),S^\beta(\vec{x}')\} = g\sum_\gamma \epsilon^{\alpha\beta\gamma}\,\phi^\gamma(\vec{x})\,\delta(\vec{x}-\vec{x}')$, one thus arrives at the coupled model G Langevin equations [4, 19, 20, 21, 35]

$$\frac{\partial\vec{\phi}(\vec{x},t)}{\partial t} = g\,\vec{\phi}(\vec{x},t)\times\frac{\delta\mathcal{H}[\vec{\phi},\vec{S}]}{\delta\vec{S}(\vec{x},t)} - \lambda\,\frac{\delta\mathcal{H}[\vec{\phi},\vec{S}]}{\delta\vec{\phi}(\vec{x},t)} + \vec{\zeta}_\phi(\vec{x},t)\ , \tag{3.9}$$

$$\begin{aligned}\frac{\partial\vec{S}(\vec{x},t)}{\partial t} &= g\,\vec{S}(\vec{x},t)\times\frac{\delta\mathcal{H}[\vec{\phi},\vec{S}]}{\delta\vec{S}(\vec{x},t)} - g\,\vec{\phi}(\vec{x},t)\times\frac{\delta\mathcal{H}[\vec{\phi},\vec{S}]}{\delta\vec{\phi}(\vec{x},t)}\\ &\quad + D\,\nabla^2\,\frac{\delta\mathcal{H}[\vec{\phi},\vec{S}]}{\delta\vec{S}(\vec{x},t)} + \vec{\zeta}_S(\vec{x},t)\ .\end{aligned} \tag{3.10}$$

One way to numerically characterize the critical dynamics of the system is to solve these coarse-grained non-linear stochastic PDEs in time and space. A more precise alternative would be to simulate the exact microscopic model of the system incorpo-

rating both the reversible and relaxational dynamics.

3.2.2 Microscopic Dynamics

At zero temperature, the microscopic spin variables at each lattice site i obey the coupled Heisenberg equations of motion $dS_i^\alpha(t)/dt = \{\mathcal{H}, S_i^\alpha(t)\}$, where the spin vector components satisfy the standard angular momentum Poisson brackets $\{S_i^\alpha, S_j^\beta\} = \sum_\gamma \epsilon^{\alpha\beta\gamma}\, S_i^\gamma\, \delta_{ij}$ with the fully antisymmetric unit tensor $\epsilon^{\alpha\beta\gamma} = \pm 1$ for $(\alpha, \beta, \gamma) = (x, y, z)$ and (z, y, x), respectively, and cyclic permutations of these coordinate indices. Hence one obtains $3L^3$ coupled deterministic equations of motion representing the spin vectors precessing in their local effective fields [37],

$$\frac{d\vec{S}_i(t)}{dt} = \vec{S}_i(t) \times \frac{\partial \mathcal{H}}{\partial \vec{S}_i(t)} \ . \tag{3.11}$$

Numerically, these reversible equations of motion for individual spins are readily integrated simultaneously [25, 26], e.g., using fourth-order predictor-corrector methods.

At non-zero temperature, one must supplement this dynamics with an appropriate relaxational kinetics that however preserves the total magnetization. One efficient means is to employ Kawasaki Monte Carlo kinetics, wherein the lattice configuration is stochastically updated by exchanging neighboring spins subject to standard Metropolis rules [38]. Yet the conservation law for the total magnetization is satisfied only within truncation error bounds set by the numerical integration scheme; in addition, one needs to adequately balance the integration time steps with a suitable number of concurrent Kawasaki spin exchange processes. We determined the integration time increment $\Delta t = 0.01/J$ to be optimal, with each numerical integration step separated by ten Monte Carlo sweeps over the entire lattice; we shall refer to this combination as one simulation time step (STS).

3.3 Numerical results

3.3.1 Dynamical critical exponent

The dynamical critical exponent for isotropic Heisenberg ferromagnets $z \approx 2.48$ [26, 39] and antiferromagnets $z = 1.5$ [40, 41] in three dimensions were numerically

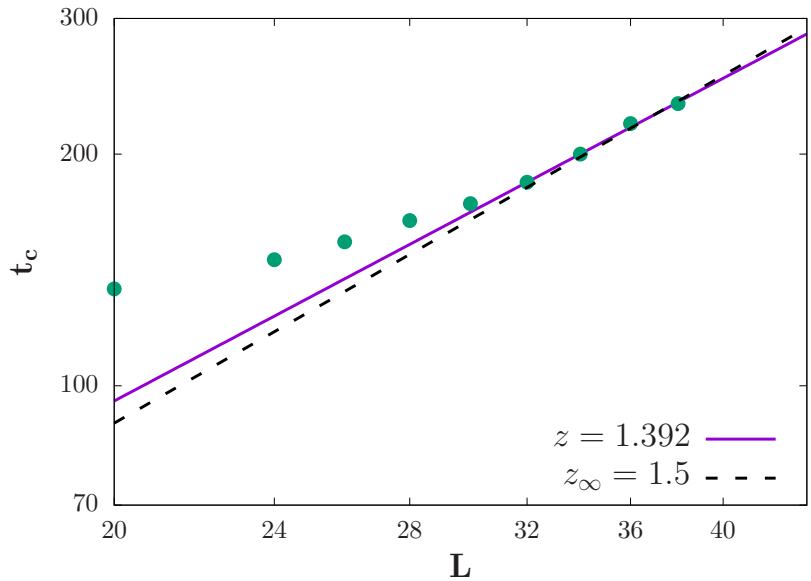

Figure 3.1: Double-logarithmic plot of the relaxation time $t_c(L)$ vs. linear system sizes $L = 20 \ldots 38$. The data points approach the exact asymptotic value $z = 1.5$ only for large L. The best fit for the last four data points ($L \geq 32$) yields $z = 1.392(10)$. (Statistical error bars are smaller than the symbol sizes.)

confirmed by means of such hybrid algorithms with remarkable accuracy, despite the major challenges imposed by the inevitable critical slowing-down, i.e., rapidly increasing relaxation time upon approaching criticality. In these studies, the temporal evolutions of the spins were determined by integrating the coupled equations of motion, but observations were made only on equilibrium configurations. Alternatively, one may probe dynamical critical behavior effectively in the earlier non-equilibrium relaxation regime following an instantaneous temperature quench from $T \gg T_c$ to the critical point [11, 16, 17, 27, 28].

In finite systems near T_c^∞, the behavior of the stationary autocorrelation function can be approximated by an exponential decay $C(t) \sim e^{-t/t_c(L)}$ [42], where the relaxation time $t_c(L) \sim L^z$ diverges with system size with the dynamic critical exponent z. We extracted the relaxation time from our $C(t)$ data for different linear system sizes L (Fig. 3.1), and found $z = 1.392(10)$ for $L \geq 32$ which is close to the exact asymptotic value $z = 1.5$ for model G.

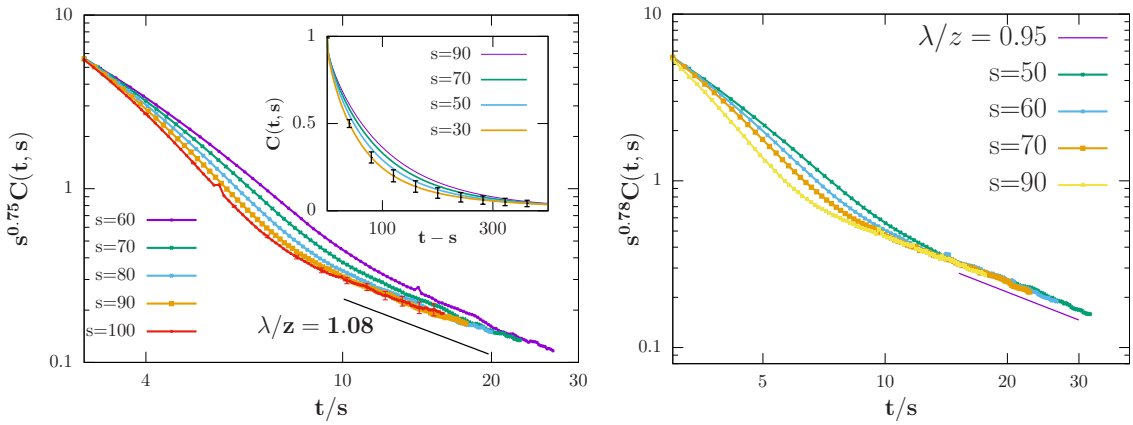

(a) (b)

Figure 3.2: (a) Aging scaling plots for the two-time spin autocorrelation function $C(t,s)$ following a quench to the critical temperature T_c^∞ on a cubic lattice with 70^3 sites. The data for each graph were averaged over 700 independent realizations. Double-logarithmic rescaled plots for $C(t,s)$ at different waiting times s collapse with the aging exponent $b = 0.75 \pm 0.04$; the corresponding decay exponent for a uniform initial distribution is $\lambda/z = 1.08 \pm 0.05$. Inset: unscaled spin autocorrelations as function of $t-s$ for various s, demonstrating broken time translation invariance. Statistical errors are indicated (inset: graph for $s = 30$, main plot: graph for $s = 100$) and are of similar size for all reported spin autocorrelations. (b) Double-logarithmic plot of $C(t,s)$ as function of the ratio t/s for various waiting times s for a smaller simulation domain with $L = 40$.

3.3.2 Critical aging scaling

In our simulations, we used truncated Gaussian distributions of varying widths σ for the orientations (on the three-dimensional unit sphere) of the initial spin configurations, and observed the decay of the two-time spin autocorrelation function

$$C(t,s) = L^{-3} \sum_i \left[\langle S_i(t)\, S_i(s) \rangle - \langle S_i \rangle^2 \right]; \tag{3.12}$$

note that this quantity measures the autocorrelations for both the staggered magnetization order parameter and the conserved magnetization. We performed critical quenches from a disordered high-temperature initial configuration to $k_B T_c^\infty / J = 1.446$ on a lattice of 70^3 spins. We observed an aging scaling time window for wait-

ing times $s = 30 \ldots 100$ STS, which allowed us to extract the aging scaling exponents b and λ/z by collapsing the tails of the non-equilibrium relaxation data for $C(t, s)$ according to Eq. (3.2). A flat orientation distribution with large σ pertains to the setup in the renormalization group analysis of Ref. [30], which instead assumed a Gaussian distribution of width c_0 for the magnitudes of the magnetization vector field. We note that while our Heisenberg spin model simulations were performed at fixed $\vec{S}_i^2 = 1$, coarse-graining over sufficiently many spins with randomized orientations over a finite lattice volume would also induce a non-zero width $c_0 > 0$ for the magnitude distribution of the resulting continuous local magnetization density.

For a uniform initial orientation distribution, we obtain a collapse exponent $b = 0.75 \pm 0.04$ for the two longest waiting times in our simulation as shown in Fig. 3.2a, while the data for shorter waiting times s start collapsing at this value near the large t/s tail of the graph. It is arguable from the data that if both longer waiting and observation times were accessible to us, we would have observed a clearer scaling collapse. This is evident from the aging scaling data for smaller linear system size $L = 40$ displayed in Fig. 3.2b, where one discerns a much better data collapse already at smaller t/s ratio.

While the asymptotic aging exponent should be $b \approx 0.69$, for our system with $L = 70$ we observe a larger value from which we infer $z = (1+\eta)/b \approx 1.38$ in good agreement with the corresponding dynamic exponent extracted from the simulation data in Fig. 3.1. To perform a more systematic finite system size analysis, we plot the exponent $b(L)$ for four different simulation samples with linear sizes $L = 40, 60, 70,$ and 100 vs. $1/L$ and linearly extrapolate the graph to estimate the asymptotic b_∞ in the thermodynamic limit ($L \to \infty$), as displayed in Fig. 3.3a. Thus we obtain $b_\infty = 0.689 \pm 0.02$ which is in excellent agreement with the theoretical prediction. We have carried out a similar extrapolation in Fig. 3.3b for the autocorrelation decay exponent λ/z to estimate its asymptotic value 1.205 ± 0.03.

For narrow distributions ($\sigma < 0.4$), we observe transient oscillations and very slow decay (Fig. 3.4a inset). We attribute these features to the formation of metastable locally ordered domains; a small range of initial orientations stabilizes the domains in a finite system and prevents large-scale relaxation processes. But for broader distributions, we clearly detect non-universal relaxation as characterized by varying exponents $\lambda(\sigma)$ and hence $\theta(\sigma)$ (Fig. 3.4a, main panel); as listed in Table I, we observe $\lambda(\sigma)$ to decrease and $\theta(\sigma)$ to increase with growing width. In contrast, within our systematic and statistical errors we find identical values for the aging collapse scaling exponent $b \approx 0.75$ for all implemented orientation distribution widths; Fig. 3.4b exemplifies this for $\sigma = 0.55$.

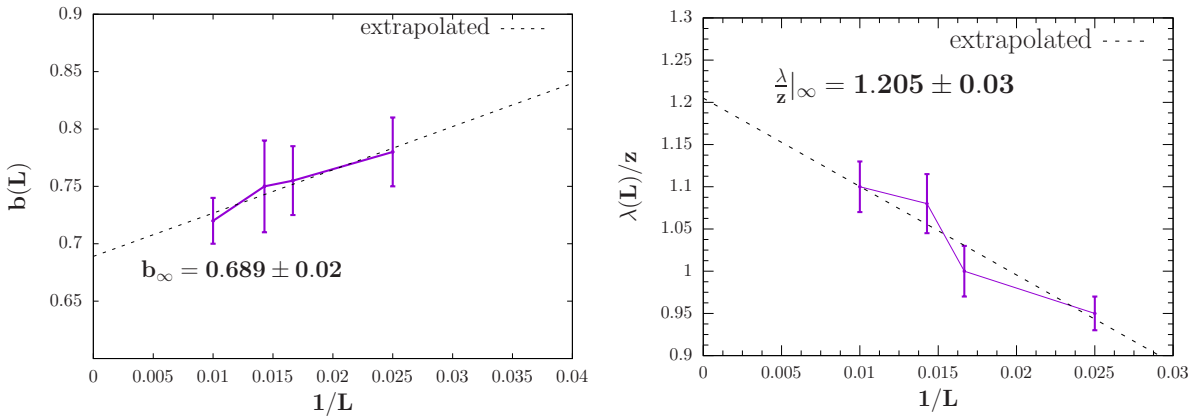

(a) (b)

Figure 3.3: Finite-size (a) aging scaling exponents b and (b) autocorrelation decay exponents λ/z plotted as functions of $1/L$ for linear system sizes $L = 40, 60, 70, 100$. The asymptotic values in the thermodynamic limit $L \to \infty$ resulting from linear extrapolation are $b_\infty = 0.689 \pm 0.02$ and $(\lambda/z)_\infty = 1.205 \pm 0.03$.

As is evident from the above table, the asymptotic value of exponents $\lambda(\sigma)/z$ for the narrower spin orientation distributions is much higher than the asymptotic value for this exponent for uniform distributions. Hence we confirm that this observation indeed clearly indicates non-universal behavior and does not result from finite-size effects.

Table 3.1: The critical aging collapse, decay, and initial-slip exponents b, λ/z, and θ measured in numerical simulations using Gaussian initial spin orientation distributions with varying width σ.

σ	b	λ/z	θ
0.5	0.73(3)	1.503(70)	0.663
0.52	0.75(5)	1.334(30)	0.785
0.55	0.77(2)	1.16(7)	0.910
uniform	0.75(4)	1.08(5)	0.955

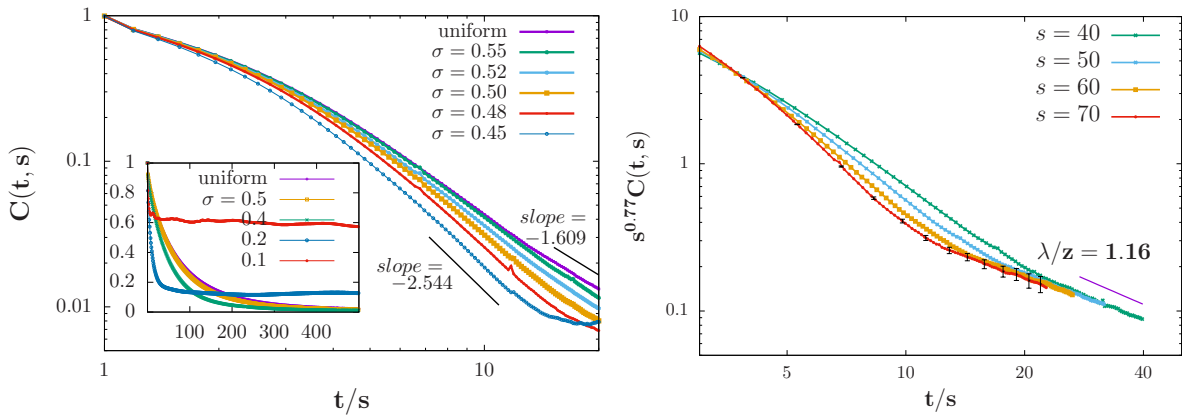

(a) (b)

Figure 3.4: Double-logarithmic plots of $C(t,s)$ as function of the ratio t/s for (a) different initial distribution widths σ at fixed waiting time s, demonstrating that the algebraic long-time decay is non-universal. Inset: time evolution of the two-time spin autocorrelation function $C(t,s)$ vs. $t-s$ for different widths σ of the initial truncated Gaussian spin orientation distribution. The data for narrow σ show distinct temporal oscillations. (b) for initial orientation distribution width $\sigma = 0.55$, yielding a collapse exponent $b = 0.77 \pm 0.02$ and decay exponent $\lambda(\sigma)/z = 1.16 \pm 0.07$. Statistical errors are indicated in the graph for $s = 70$.

3.4 Concluding remarks

In summary, we have employed a hybrid numerical algorithm that combines reversible spin precession with relaxational kinetics implemented through Kawasaki spin exchange processes to study the critical dynamics of isotropic Heisenberg antiferromagnets on a three-dimensional simple cubic lattice. Within systematic errors, our data for the characteristic spin autocorrelation relaxation time are in agreement with the dynamic critical exponent $z = 3/2$ for the model G universality class, where a non-conserved three-component order parameter (here, the staggered magnetization) is dynamically coupled to a conserved non-critical vector field (the magnetization). Furthermore, we have investigated the non-equilibrium relaxation kinetics of isotropic antiferromagnets following a critical quench. We obtain a universal value $b \approx 0.75$ for the critical aging scaling collapse exponent, which within the errors of our simulation as reflected in the measurement of z conforms with the asymptotic value $b \approx 0.69$. We have also performed a finite-size extrapolation analysis with four different linear system sizes, which yielded the correct asymptotic value of the

critical aging scaling exponent $b \approx 0.689$.

Additionally, we have demonstrated that for isotropic antiferromagnets, the autocorrelation decay λ/z and hence the initial-slip exponent θ intriguingly depend on the width σ of the Gaussian distribution for the initial spin orientations, and hence represent non-universal critical scaling exponents. This remarkable and quite unusual feature was predicted by Oerding and Janssen [30]; in a one-loop perturbative dynamical renormalization group analysis, they found an explicit dependence of the critical initial-slip exponent θ on the width of the initial Gaussian distribution c_0 for the magnitude of the magnetization vector. Our present numerical study that utilized different initial Gaussian distributions for the spin vector orientations thus validates this intriguing and unusual prediction; in accord with Ref. [30], we furthermore obtain universal values for λ and θ in the limit of sufficiently wide orientation distributions. It would be interesting to characterize this striking non-universal behavior further by utilizing non-Gaussian initial spin distributions. The efficient numerical simulation technique described above can also be used to explore critical short-time dynamics of more complex anisotropic antiferromagnets subject to external fields, which exhibit several distinct phase transition lines and hence allow for the presence of multi-critical points [43].

In closing we note that we have performed similar dynamical simulations for isotropic Heisenberg ferromagnets on a three-dimensional lattice. However, probably owing to the much slower critical relaxation with dynamic exponent $z = (5-\eta)/2 \approx 2.48$, we were not able to access a sufficiently large aging time window before finite-size effects began to dominate and cut off the expected universal power laws with the universal model J scaling exponents $b = 2(1+\eta)/(5-\eta) \approx 0.42$, $\lambda = 5$, and $\theta = -(3-\eta)/(5-\eta) \approx -0.60$ in three dimensions.

3.5 Appendix

3.5.1 Microscopic Equations of Motion

The Hamiltonian of a three-dimensional isotropic antiferromagnet with Heisenberg interaction is given by,

$$\mathcal{H} = -J \sum_{<ij>} \vec{S}_i \cdot \vec{S}_j \ . \tag{3.13}$$

where $< ij >$ are the nearest neighbor spins. The microscopic equations of motion governing each spin vector at zero temperature are,

$$\frac{d\vec{S}_i}{dt} = \{\vec{S}_i, \mathcal{H}\} \ . \tag{3.14}$$

Thus for each component of spin vector, using the standard Poisson bracket relation among the spin angular momentum components $\{S_i^\alpha, S_j^\beta\} = \delta_{ij}\epsilon^{\alpha\beta\gamma}S_i^\gamma$, one obtains,

$$\begin{aligned}
\{S_i^\alpha, \mathcal{H}\} &= -J\{S_i^\alpha, \sum_{<ij>}(S_i^\alpha S_j^\alpha + S_i^\beta S_j^\beta + S_i^\gamma S_j^\gamma)\} \\
&= -J\Big[\Big\{S_i^\alpha, S_i^\beta\Big\}\sum_j S_j^\beta + \Big\{S_i^\alpha, S_i^\gamma\Big\}\sum_j S_j^\gamma\Big] \\
&= -J\Big(\epsilon^{\alpha\beta\gamma}S_i^\gamma\sum_j S_j^\beta + \epsilon^{\alpha\beta\gamma}S_i^\beta\sum_j S_j^\gamma\Big) \\
&= \epsilon^{\alpha\beta\gamma}S_i^\gamma\nabla_i^\beta\mathcal{H} - \epsilon^{\alpha\beta\gamma}S_i^\beta\nabla_i^\gamma\mathcal{H} \\
&= \Big(\vec{S}_i \times \vec{\nabla}\mathcal{H}\Big)^\alpha
\end{aligned} \tag{3.15}$$

Therefore, we arrive at the equations of motion for the microscopic spin vectors that ensure their precession around a local field produced by their nearest neighbors implied by the spatial derivative of the Hamiltonian,

$$\frac{d\vec{S}}{dt} = \vec{S} \times \vec{\nabla}\mathcal{H} \ . \tag{3.16}$$

For the ease of computation we work with the spherical polar coordinates where the Cartesian components of the spin vector are related to the azimuthal and polar angles via $(S^x, S^y, S^z) = (\sin\vartheta\cos\varphi, \sin\vartheta\sin\varphi, \cos\vartheta)$ and the magnitude of each spin vector is fixed to unity, $(S_i^x)^2 + (S_i^y)^2 + (S_i^z)^2 = 1$. Thus, solving for the z-component of the spin vector we get,

$$\frac{dS_i^z}{dt} = \frac{d}{dt}\cos\vartheta_i = -\sin\vartheta_i\frac{d\vartheta_i}{dt} \tag{3.17}$$

From Eqn. 3.15,

$$\begin{aligned}\frac{dS_i^z}{dt} &= J\Big(S_i^y \sum_j S_j^x - S_i^x \sum_j S_j^y\Big) \\ &= J\sin\vartheta_i\Big(\sin\varphi_i \sum_j \sin\vartheta_j \cos\varphi_j - \cos\varphi_i \sum_j \sin\vartheta_j \sin\varphi_j\Big)\end{aligned}$$

Equating the above two equations gives the equation of motion for the azimuthal angle,

$$\frac{d\vartheta_i}{dt} = -J\sum_j \sin\vartheta_j(\sin\varphi_i\cos\varphi_j - \cos\varphi_i\sin\varphi_j) = -J\sum_j \sin\vartheta_j \sin(\varphi_i - \varphi_j) \quad (3.18)$$

Similarly, solving for the x-component we get,

$$\frac{dS_i^x}{dt} = \frac{d}{dt}\sin\vartheta_i\cos\varphi_i = \cos\vartheta_i\cos\varphi_i\frac{d\vartheta_i}{dt} - \sin\vartheta_i\sin\varphi_i\frac{d\varphi_i}{dt} \quad (3.19)$$

From Eqn. 3.15,

$$\frac{dS_i^x}{dt} = J\Big(S_i^z\sum_j S_j^y - S_i^y\sum_j S_j^z\Big) = J\Big(\cos\vartheta_i\sum_j \sin\vartheta_j\sin\varphi_j - \sin\vartheta_i\sin\varphi_i\sum_j\cos\vartheta_j\Big)$$

Therefore, from the above two equations,

$$\begin{aligned}\sin\vartheta_i\sin\varphi_i\frac{d\varphi_i}{dt} &= -J\cos\vartheta_i\cos\varphi_i\sum_j\sin\vartheta_j\sin(\varphi_i-\varphi_j) \\ &- J\Big(\cos\vartheta_i\sum_j\sin\vartheta_j\sin\varphi_j - \sin\vartheta_i\sin\varphi_i\sum_j\cos\vartheta_j\Big)\end{aligned}$$

Rearranging the left and right hand sides,

$$\begin{aligned}
\frac{d\varphi_i}{dt} &= J\sum_j \cos\vartheta_j - J\cot\vartheta_i \sum_j \sin\vartheta_j \Big(\frac{\sin\varphi_j}{\sin\varphi_i} + \frac{\cos\varphi_i}{\sin\varphi_i}[\sin\varphi_i\cos\varphi_j - \cos\varphi_i\sin\varphi_j]\Big) \\
&= J\sum_j \cos\vartheta_j - J\cot\vartheta_i \sum_j \sin\vartheta_j \Big(\cos\varphi_i\cos\varphi_j + (1-\cos^2\varphi_i)\frac{\sin\varphi_j}{\sin\varphi_i}\Big) \\
&= J\sum_j \cos\vartheta_j - J\cot\vartheta_i \sum_j \sin\vartheta_j \Big(\cos\varphi_i\cos\varphi_j + \sin\varphi_i\sin\varphi_j\Big)
\end{aligned}$$

Thus, the equations of motion for the polar angle is given by,

$$\frac{d\varphi_i}{dt} = J\sum_j \cos\vartheta_j - J\cot\vartheta_i \sum_j \sin\vartheta_j \cos(\varphi_i - \varphi_j) \tag{3.20}$$

3.5.2 Hybrid Simulation Method

The hybrid simulation algorithm employed in order to equilibriate the system of antiferromagents as described in sections 3.2.2 is outlined below.

- In order to relax the system towards equilibrium at the temperature of the quench, perform the Monte Carlo update algorithm:
  - Select a spin variable at a random lattice site denoted by i, j, and k.
  - If the total magnetization is conserved by the microscopic Hamiltonian as in section 3.2.2, employ the Kawasaki spin exchange method [38] to update the spins:
    1. In a simple cubic lattice with periodic boundary conditions, each spin has six neighboring spins. Select a random neighboring spin with probability 1/6.
    2. Calculate the energy difference ΔE if the position of the two spins are exchanged in the lattice.
    3. Define the probability of exchange as $W = \exp(-\Delta E/k_B T)$, where T is the temperature at which the system equilibriates after long times.
    4. Generate a random number r from a uniform distribution between 0 and 1.
    5. If $r < W$, exchange the two spins.

- In order to simulate the precession of the spin variables which result in reversible dynamics, integrate the equations of motion of the azimuthal and polar angles of the spins, Eqns. 3.18 and 3.20 respectively at each lattice site.
- Update the lattice configuration with 10 sweeps of the Monte Carlo algorithm and then parallelly integrate all the spins by implementing 4th order Runge-Kutta algorithm. This combination is defined as one simulation time step (STS).

The ratio between the Monte Carlo update and the integration update is represented by the ratio of the coupling constant g and the diffusivity D in the mesoscopic eqn. 3.10. Renormalization group analysis leads to this ratio being irrelevant at the fixed point, or at the critical parameters. However, our simulations are performed on finite length and time scales. Hence, choosing the right ratio is imperative to obtain the correct dynamics. Our simulation data is insensitive to the variation of this ratio by less than an order of magnitude. Increasing the number of integration steps per simulation step by an order of magnitude leads to a faster relaxation process where the dynamics is washed out and the system starts to observe finite-size effects very early. Increasing the number of Monte Carlo updates makes the dynamics much slower.

Chapter 4

Critical Dynamics of Anisotropic Antiferromagnets in an External Field

This chapter is adapted from our publication [44],
Riya Nandi and Uwe C. Täuber, "Critical Dynamics of Anisotropic Antiferromagnets in an External Field", Phys. Rev. E (2020) 102, 052114, Copyright (2020) by the American Physical Society.

My contributions to this publication include developing the simulation algorithm, analysing the obtained data, and preparing the first draft of the manuscript including the figures.

4.1 Introduction

Classical anisotropic antiferromagnets governed by Heisenberg spin exchange in an external magnetic field exhibit a rich phase diagram with multiple thermodynamic ground states separated by continuous and discontinuous transition lines that meet at a multicritical point [45, 46]. This paradigmatic model system describes various magnetic compounds including MnF_2 [47], $GdAlO_3$ [48], $NiCl_2 \cdot 6H_2O$ [49], and thus has been extensively investigated theoretically as well as experimentally. Early renormalization group [50], Monte Carlo simulation [43], and high-temperature expansion [51] studies have systematically explored its complex phase diagram and characterized the properties of the different ordered phases and determined the universality classes for its critical transition lines.

The anisotropy term along one of the crystal axes breaks the rotational symmetry of the Heisenberg antiferromagnet enforcing an antiparallel spin ordering along that

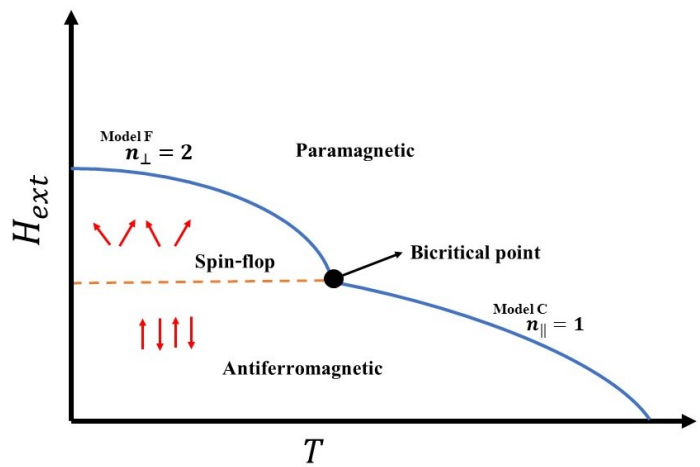

Figure 4.1: Schematic H_{ext}-T phase diagram of an anisotropic antiferromagnet in the presence of an external field showing two ordered phases separated by a first-order transition line. The antiferromagnetic and spin-flopped ordered phases are separated from the disordered paramagnetic phase by lines of continuous phase transitions that meet at a bicritical point.

axis in the low-temperature, low-field ground state, i.e., the Ising antiferromagnetic phase (AF), c.f. Fig. 4.1. As the external field strength is tuned up while keeping the temperature low, the ground state switches, via a discontinuous (first-order) transition, to a spin-flop phase (SF). At higher values of either temperature or magnetic field, the system becomes paramagnetic (PM). The phase transitions between the PM and the AF and SF states are both continuous (second-order). While the associated static critical properties of the system are characterized solely by the symmetry and the dimensionality of the anisotropic Heisenberg Hamiltonian, the dynamics in the vicinity of the phase transitions driving it from the disordered phase to the ordered AF and SF phases, respectively, are distinctly different and crucially depend on the microscopic, reversible dynamical couplings between the corresponding order parameters and the conserved magnetization components.

Indeed, the transition from the antiferromagnetic to the paramagnetic phase is described by the dynamic critical behavior of model C, while the spin-flop to paramagnetic phase transition belongs to the dynamical universality class of model F; here we invoke the classification introduced by Halperin and Hohenberg in 1977 in their comprehensive early review of dynamic critical phenomena [4]. The presence

of a non-ordering field shifts the non-universal parameters of the system such as the critical temperature, but it does not change the nature of the critical point, i.e, the universal scaling exponents characterizing the critical power law divergences remain unaltered. Yet an intriguing distinct physical scenario results in the vicinity of the *multicritical point*, where both critical lines as well as the discontinuous phase transition meet. At the multicritical point, all three different phases compete for the lowest free energy configuration; thus the system's symmetry at this special point is higher than in the adjacent parameter space. Hence, the dynamical properties in the vicinity of such a point are expected to be characterized by new exponents which are distinct from those of the conjoining critical lines.

The nature of the multicritical point for anisotropic antiferromagnets subject to an external magnetic field (oriented along the z direction) has been somewhat controversial. This special point in parameter space is characterized by two coupled order parameter fields with $O(n_\perp) \bigoplus O(n_\parallel)$ symmetry; it displays long-range order both along the magnetic field z axis and in the perpendicular xy plane. A series of papers by Folk, Holovatch, and Moser employed the renormalization group to investigate the static and dynamic critical behavior and the stability of the associated fixed points of the system [52, 53, 54, 55]. They predicted the emergence of either bicritical behavior associated with a Heisenberg fixed point or tetracritical behavior, in turn associated with a biconical or a decoupled renormalization group fixed point. An analysis to higher order resulted in the tetracritical point with a biconical phase to represent the stable fixed point [56]. Subsequently, a full renormalization group study of the flow equations at the multicritical point taking into account the reversible terms concluded that in two-loop order the biconical fixed point becomes stable, whereas the Heisenberg fixed remains stable in a one-loop calculation [55]. In contrast, a series of detailed Monte Carlo simulations analyzing order parameter susceptibilities, the Binder cumulant, and associated probability distributions provided concrete evidence that the nature of the multicritical point is in fact *bicritical* with Heisenberg symmetry [57, 58].

While the static critical behavior and stationary critical dynamics of this system has been investigated comprehensively in the literature, we are not aware of previous computational work addressing the non-equilibrium critical relaxation of the anisotropic Heisenberg antiferromagnet in an external magnetic field near either continuous phase transition line, nor at the multicritical point. To this end, the system is initially prepared in at a disordered configuration and then quenched precisely to its critical point such that the dynamics algebraically slowly evolves towards the asymptotic stationary state. During this early non-equilibrium relaxation time win-

dow, the system retains the memory of its initial state, and thus manifests broken time translation invariance. By studying the ensuing aging scaling behavior of two-time quantities at these early times, one may fully characterize the dynamics near the distinct critical points and the corresponding universality classes [11, 17].

In this work, we utilize a hybrid simulation method combining relaxational Monte Carlo kinetics and reversible spin precession processes [18] to explore the aging scaling behavior of the AF-to-PM model C critical line, and in the vicinity of the multicritical point. We measure the critical aging scaling, autocorrelation decay, and initial slip exponents for the model C universality class, and determine the associated dynamic critical exponent. We also investigate the non-equilibrium dynamics of the conserved magnetization component. Furthermore, we utilize Fourier spectral analysis for the spin wave excitations in the xy plane in the spin-flop ordered phase to verify the dynamic critical exponent for the SF-to-PM model F critical line. Finally, we investigate the critical order parameter dynamics at the bicritical point.

4.2 Model and Simulation Method

The Hamiltonian of a three-dimensional antiferromagnet with anisotropic Heisenberg exchange interactions in an external magnetic field is given by

$$\mathcal{H} = J \sum_{\langle ij \rangle}^{N} \left[\Delta (S_i^x S_j^x + S_i^y S_j^y) + S_i^z S_j^z \right] - H_{\text{ext}} \sum_{i=0}^{N} S_i^z \,, \tag{4.1}$$

where S_x^i, S_y^i, S_z^i represent the components of the three-dimensional spin vector $\vec{S}^i$ at the ith site of a simple cubic lattice of linear extension L with total spin number $N = L^3$. The magnitude of the spins are fixed to unit magnitude, $S_x^{i2} + S_y^{i2} + S_z^{i2} = 1$. $J > 0$ denotes the antiferromagnetic exchange interaction along the z axis between nearest-neighbor spin pairs $\langle ij \rangle$; we set $J = +1$, i.e., measure temperature in units of J/k_{B} and the external field in units of J. The uniaxial anisotropy $0 < \Delta < 1$ imposes an "easy" z axis such that the spins would order anti-parallel along this direction in the absence of an external field [57]; we choose $\Delta = 0.8$. The presence of this anisotropy explicitly breaks the $O(3)$ rotational symmetry of the Hamiltonian in spin space and splits it into two subspaces of dimensions $n_{\parallel} = 1$ and $n_{\perp} = 2$. Thus its static critical properties are governed by the universality class with $O(1) \bigoplus O(2)$ symmetry with associated Fisher exponent $\eta \approx 0.04$ [52].

Applying an external magnetic field $H_{\text{ext}} \neq 0$ along the z axis forces the uniaxially aligned spins to flop over into the xy plane beyond some critical field strength H^c_{ext}. Thus, at low temperature T and external field H_{ext}, i.e. in the AF phase, the z component of the staggered magnetization

$$\phi_{\parallel} = \sum_{i,j,k=0}^{L} (-1)^p S^z_{i,j,k} \tag{4.2}$$

represents the non-conserved order parameter for the system; here the indices (i, j, k) denote the three spatial directions, and $p = i + j + k$ ensures that the sum extends over the differences between every alternate spin in the lattice. Upon increasing H_{ext}, the value of $\phi_{\parallel}$ is diminished, and instead the staggered magnetization components in the xy plane perpendicular to the applied field become appreciable. Thus in the SF phase, an appropriate, also non-conserved, order parameter is a two-component vector $\vec{\phi}_{\perp} = (\phi_x, \phi_y)$ with magnitude

$$\phi_{\perp} = \sqrt{\left(\sum_{i,j,k=0}^{L} (-1)^p S^x_{i,j,k}\right)^2 + \left(\sum_{i,j,k=0}^{L} (-1)^p S^y_{i,j,k}\right)^2}\,. \tag{4.3}$$

It is important to note that the Hamiltonian (4.1) conserves the z component of the total magnetization

$$M_z = \sum_{i,j,k=0}^{N} S^z_{i,j,k} \tag{4.4}$$

under the dynamics, $\{\mathcal{H}, M_z\} = 0$; here the Poisson bracket constitutes the classical counterpart of the quantum-mechanical commutation relation between the spin angular momentum and the Hamiltonian. The dynamical mode couplings between conserved magnetization fluctuations and the order parameter components decisively influence the antiferromagnet's critical dynamics [4, 9, 11, 21]. Indeed, in addition to the irreversible, relaxational terms arising from the static couplings in the Hamiltonian, one must account for the *reversible* kinetics caused by the underlying microscopic dynamics between the order parameter and any conserved modes. At zero temperature, the microscopic equations of motion obeyed by each spin variable are $dS^{\alpha}_i(t)/dt = \{\mathcal{H}, S^{\alpha}_i(t)\}$, where the spin vector components satisfy the standard angular momentum Poisson brackets $\{S^{\alpha}_i, S^{\beta}_j\} = \sum_{\gamma} \epsilon^{\alpha\beta\gamma}\, S^{\gamma}_i\, \delta_{ij}$ with the fully antisymmetric unit tensor $\epsilon^{\alpha\beta\gamma} = \pm 1$.

In the $n_\parallel = 1$ subspace $\{M_z, \phi_\parallel\} = 0$; thus there is no reversible coupling term. However, in the $n_\perp = 2$ subspace, the non-conserved vector order parameter $\vec{\phi}_\perp (= \phi_x, \phi_y)$ couples reversibly to the conserved magnetization (4.4)

$$\{M_z, \phi_\alpha\} = \epsilon_{\alpha\beta z}\phi_\beta \tag{4.5}$$

where $\alpha, \beta \in \{x, y\}$. This non-vanishing mode coupling gives rise to the following deterministic equations of motion of the microscopic spin components at $T = 0$ [21, 37]

$$\frac{d\vec{S}_i(t)}{dt} = \vec{S}_i(t) \times \frac{\partial \mathcal{H}}{\partial \vec{S}_i(t)} \ , \tag{4.6}$$

which describe precession of the unit spin vector in the local effective field.

To simulate the dynamics of this system at finite temperature, one needs to implement relaxation terms as well as the reversible microscopic equations of motion. For convenience, we work with the two angular degrees of freedom ϑ and φ that are related to the unit vector spin components through

$$(S_x, S_y, S_z) = (\sin\vartheta\cos\varphi, \sin\vartheta\sin\varphi, \cos\vartheta) \ .$$

To respect the underlying conservation property, the azimuthal angles ϑ are updated by means of Kawasaki Monte Carlo kinetics where two randomly picked neighboring spins exchange their ϑ values following the standard Metropolis rules [38]. In contrast, the polar angles φ are evolved using Glauber dynamics where the spin component at the selected lattice site is subjected to a finite rotation with again Metropolis updates [59]. These Monte Carlo update steps of the spin configurations are alternated with a fourth-order Runge-Kutta integration of the equations of motion (4.6) [18]. For our simulation, the integration was performed in parallel on all spins over discrete time increments $\Delta t = 0.01/J$ with each integration step separated by 10 Monte Carlo sweeps over the entire lattice. We determined this combination to be optimal in maintaining the conservation laws within the truncation error bounds of the numerical integration scheme.

4.3 Model C dynamical scaling

The dynamical universality class conventionally labeled as model C describes the pure relaxation dynamics of a non-conserved n-component critical order parameter

field, coupled to a conserved density [4, 9, 11, 60]. In the present study, the low-temperature, low-field ground state is an Ising antiferromagnet; hence $n = 1$ with the z-component of the magnetization density constituting the conserved scalar field m. A two-loop renormalization group calculation demonstrated that the scalar model C ($n = 1$) is governed by a strong-scaling fixed point with both the order parameter relaxation and the conserved density diffusion scaling with the same anomalous exponent α/ν [61]. This results in the *dynamic critical exponent* $z_z = z_m = 2 + \alpha/\nu \approx 2.185$; here $\nu \approx 0.72$ [62, 63] describes the algebraic divergence of the correlation length $\xi \sim |\tau|^{-\nu}$ ($\tau \sim T - T_c$), and α is the specific heat critical exponent, $C \sim |\tau|^{-\alpha}$, which can be obtained from the hyperscaling relation $\alpha = 2 - d\nu$ in d dimensions.

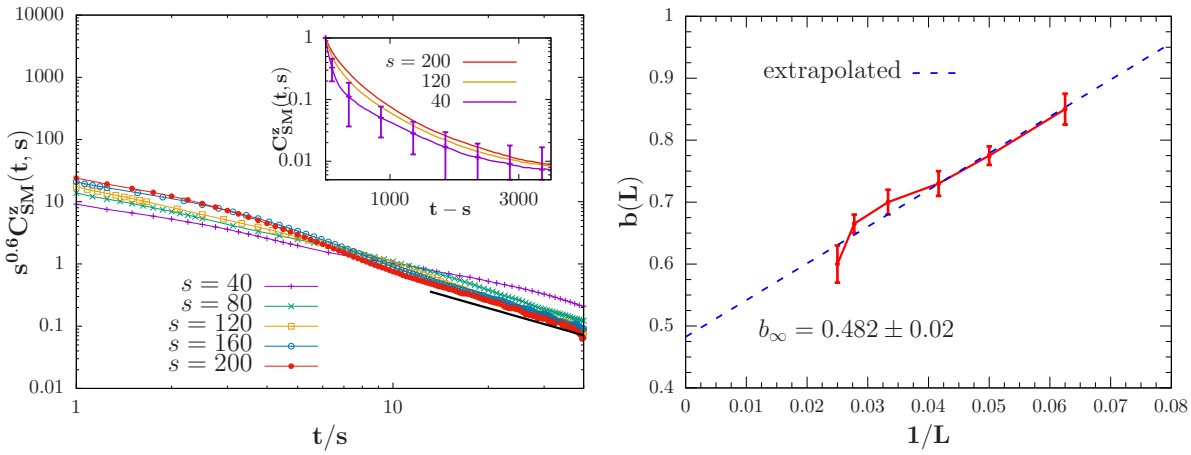

Figure 4.2: (a) Aging scaling plots for the two-time spin autocorrelation function $C^z_{\rm SM}(t,s)$ of the Ising antiferromagnetic order parameter on a simple cubic lattice of linear system size $L = 40$ with periodic boundary conditions. The system is quenched from an initially disordered configuration to the critical point at $T_c = 1.5$, $H^c_{\rm ext} = 3.0$. Double-logarithmic rescaled graphs for different waiting times s collapse with the scaling exponent $b = 0.6$. The inset shows the autocorrelation plots as a function of $t - s$ (in simulation time steps), demonstrating broken time translation invariance. Statistical errors are indicated in the graph for the shortest waiting time $s = 40$. (b) Finite-size extrapolation analysis for the aging exponent $b(L)$ plotted vs. $1/L$ for six different system sizes $L = 16 \ldots 40$. A linear extrapolation to the infinite system size limit $L \to \infty$ yields $b_\infty = 0.482 \pm 0.02$.

The non-equilibrium relaxation of model C was investigated by Oerding and Janssen using the dynamic renormalization group approach [64]. Following a critical quench,

the two-time order parameter correlation function relating two space-time points at distance r and times $s < t$ satisfies the scaling law

$$C(t, s, r, \tau) = r^{-(d-2+\eta)} \, (t/s)^{\theta-1} \, \hat{C}(r/\xi, t/\xi^z) \,, \tag{4.7}$$

where θ is the *initial slip exponent* representing a new independent universal exponent for purely dissipative systems with non-conserved order parameter [16]. It also describes the power law growth of the order parameter in the early-time universal regime which sets in right after the microscopic time during the non-equilibrium relaxation process. At the critical temperature $T = T_c$ ($\tau = 0$), the two-time autocorrelation function ($r = 0$) assumes the simple-aging scaling form [17],

$$C(t, s) \sim s^{-b} \, (t/s)^{-\lambda/z} \,, \tag{4.8}$$

with the static and dynamic exponents related to the *scaling collapse exponent* b via

$$b = (d - 2 + \eta)/z \,, \tag{4.9}$$

and to the *autocorrelation exponent* λ according to

$$\lambda = d - 2 + \eta + z(1 - \theta) = z(1 + b - \theta) \,. \tag{4.10}$$

For model C with $n = 1$, a second-order perturbative renormalization calculation predicts $\theta \approx 0.27$ in three dimensions, if one boldly extrapolates the dimensional expansion in $\epsilon = 4 - \epsilon$ to $\epsilon = 1$ [64].

To numerically study the critical relaxation and the aging scaling regime we initialized the system in a disordered spin orientation configuration corresponding to a very high temperature, and subsequently performed critical quenches to a point ($T_c = 1.5$, $H^c_{\text{ext}} = 3.0$) on the model C critical line. As shown in Fig. 4.2(a), we obtain an aging scaling window for waiting times $s = 120 \ldots 200$ simulation time steps. The inset demonstrates that time translation invariance is broken, as the two-time correlation function for the order parameter $C^z_{\text{SM}}(t, s)$ (where the subscript SM denotes the staggered magnetization) is not simply a function of the time difference $t - s$ as it would be in the stationary limit, but evolves differently for the distinct waiting times s in this temporal window. By collapsing the data of $C^z_{\text{SM}}(t, s)$ for several waiting times s plotted as a function of the time ratio t/s in accordance with Eq. (4.8), one can obtain the collapse exponent b for which we find $b \approx 0.6$ for linear system extension $L = 40$. The data collapse is noticeably improved for both later waiting times s and larger observation times t. This is expected since the simple-aging scaling form (4.8)

is supposed to hold only for sufficiently large $t \gg s$ and s.

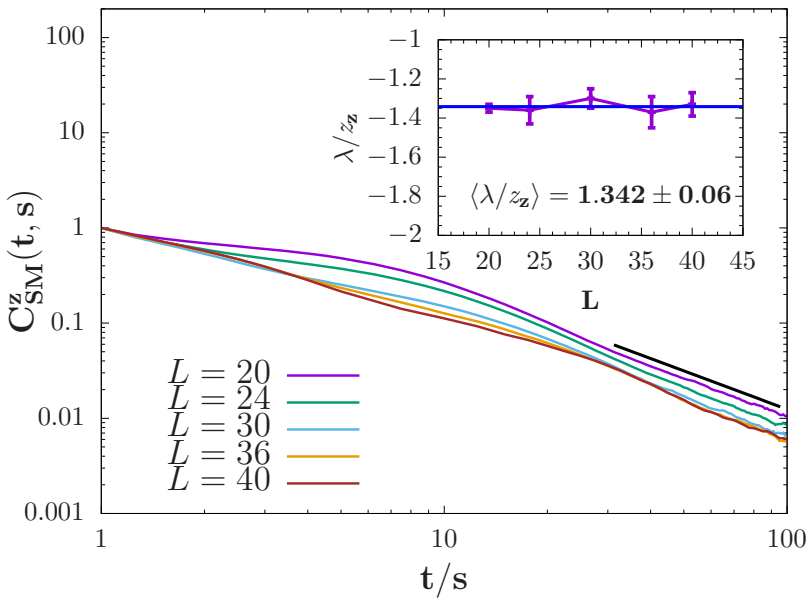

Figure 4.3: Double-logarithmic plots of the two-time staggered magnetization autocorrelation function vs. t/s for different linear system sizes L taken at an early waiting time $s = 40$ exhibit power law decays in the long-time limit $t \gg s$. The mean value of the autocorrelation exponent is determined to be $\langle\lambda/z_z\rangle = 1.342 \pm 0.06$.

However, in our finite simulation domain, data for large times are inevitably hindered by finite-size effects. Thus, in order to better estimate the asymptotic collapse exponent, we perform a systematic finite-size extrapolation analysis by plotting b vs. $1/L$ for system sizes $L = 16, 20, 24, 30, 36, 40$, c.f. Fig. 4.2(b). Linear extrapolation to infinite system size $L \to \infty$ leads to $b_\infty = 0.482 \pm 0.02$. We then obtain from Eq. (4.9) the dynamic exponent for the order parameter in model C in $d = 3$ dimensions, $z_z = (1 + \eta)/b = 2.158 \pm 0.09$. This result agrees well within our errors with the theoretically predicted value $z_z \approx 2.185$. The autocorrelation exponent λ/z_z can be extracted from the power law tails of $C^z_{\rm SM}(t, s)$, apparent in double-logarithmic plots vs. t/s for times $t \gg s$. Fig. 4.3 displays the data for five different system sizes, from which we obtain the mean value $\langle\lambda/z_z\rangle = 1.342 \pm 0.06$. Using Eq. (4.10), one may obtain the initial slip exponent $\theta = 0.14 \pm 0.08$. This value shows a similar trend as the theoretical prediction, but unsurprisingly, differs in magnitude by about a factor 2 from the naive extrapolation of the second-order results of the perturbative ϵ expansion about the mean-field value $\theta = 0$.

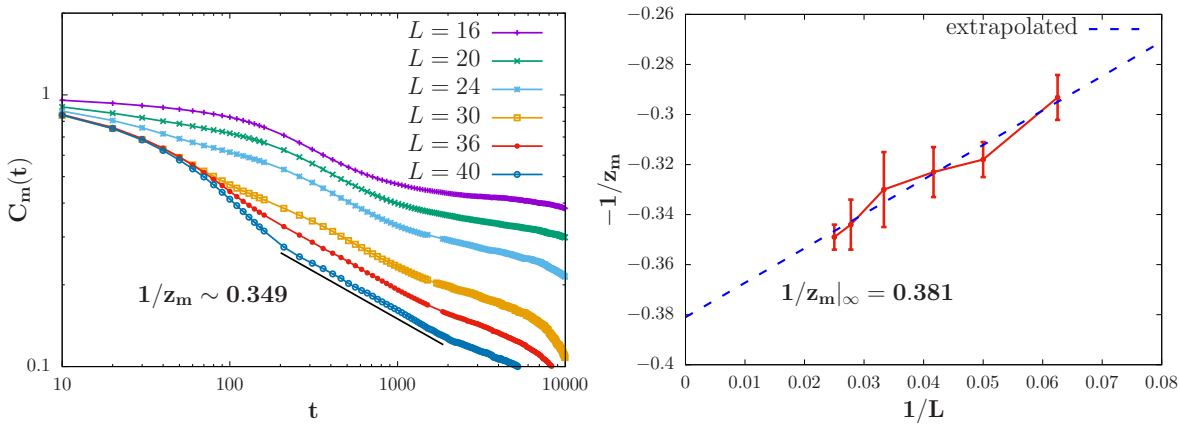

(a) (b)

Figure 4.4: (a) Double-logarithmic plots of the autocorrelation function for the conserved magnetization component M_z vs. time t for different linear system sizes L display an intermediate regime governed by algebraic decay. The system was quenched to the critical point at $T_c = 1.5$, $H^c_{\text{ext}} = 3.0$. (b) Finite-size extrapolation analysis for the decay exponent plotted vs. $1/L$ for six different system sizes $L = 16 \ldots 40$. A linear extrapolation to the infinite system size limit $L \to \infty$ yields $1/z_m = 0.381$.

We further explore the non-equilibrium dynamics of the conserved magnetization component M_z which is reversibly coupled to the ordered parameter. This non-critical conserved field undergoes diffusive relaxation with correlations $C_m(\vec{q}, \omega) \sim q^{-2}\hat{C}(\omega/q^z)$ or equivalently $C_m(\vec{r}, t) \sim r^{-(d-2)}\tilde{C}(r/t^z)$. The asymptotic long-time scaling form for the temporal magnetization correlation function at the critical temperature thus becomes

$$C_m(t) \sim t^{-(d-2)/z} \,. \tag{4.11}$$

In the data depicted in Fig. 4.4(a), we discern an intermediate power law region in the decay of the spin autocorrelation function before the graphs fall off exponentially due to finite-size effects. As expected, this algebraic regime becomes more prominent upon increasing the linear system size L. We again perform a systematic finite-size extrapolation to obtain the asymptotic value of the decay exponent and find $(1/z_m)_\infty \approx 0.381$, and thus infer $z_m \approx 2.62 \pm 0.01$. This value however differs from the order parameter dynamic exponent $z_z \approx 2.148 \pm 0.1$, indicating that likely the time-scale ratio between the staggered magnetization relaxation and magnetization diffusion still has not reached its asymptotic fixed point, and the strong dynamic scaling hypothesis cannot be validated. In this context, we direct the readers towards

previous work by Koch and Dohm discussing the effect of finite system size on the relaxation and diffusion time scales of model C [65].

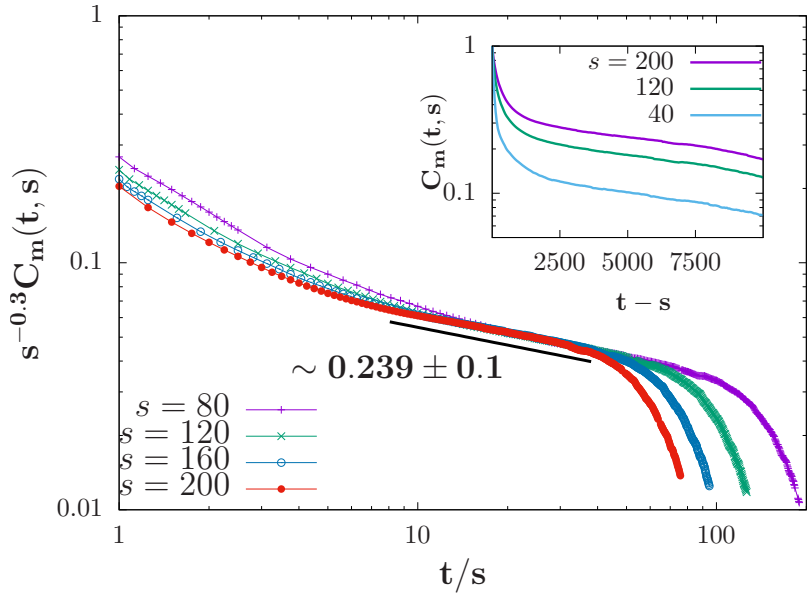

Figure 4.5: Aging scaling plots for two-time autocorrelation function $C_m(t, s)$ of the conserved magnetization for linear system size $L = 40$. Double-logarithmic rescaled plots for different waiting times s collapses with exponent $b_m \approx -0.3$ and decay exponent $\approx 0.239 \pm 0.1$. The inset shows the autocorrelation plots as a function of $t - s$ demonstrating broken time translation invariance.

One can also obtain the aging scaling data from the two-time autocorrelation function for the conserved magnetization, c.f. Fig. 4.5. We note though that for large waiting times we observe another power-law region at later times which is distinctly different from the previously obtained algebraic decay in the intermediate relaxation regime of the single-time autocorrelation function. It is at these later times that the rescaled plots for different waiting times collapse with an exponent $b_m \sim -0.3$ and a decay exponent equal to 0.239 ± 0.01. Earlier analyses of conserved spin systems have predicted two regimes with different power laws, with a new length scale governing the crossover between both algebraic regimes [29, 66]. Ultimately in the long-time limit, however, the decay of the autocorrelations is determined by only one length scale, independent of the waiting time s. In a similar vein, the non-critical conserved magnetization here displays the signature of two distinct scaling regimes. Yet unlike in the conserved spin systems, we observe an early relaxation regime with a faster

power law decay, prominent in the single-time autocorrelation plots in Fig. 4.4, which subsequently crosses over to a slower algebraic decay until ultimately finite-size effects dominate. Moreover, the negative value of the exponent b_m suggests the presence of long-lived metastable states. The precise nature of the crossover scaling for the conserved magnetization in our system thus remains open for future investigation.

4.4 Model F dynamical scaling

The continuous phase transition between the spin flop and the paramagnetic phases is described by the dynamic universality class model F [4, 9]. Also known as the "asymmetric planar spin model" [19], this universality class describes the critical dynamics of a two-component vector order parameter coupled reversibly to a conserved scalar density in the presence of an external Z_2 symmetry-breaking field. The only other known and prominent physical system described by model F is the normal- to superfluid transition in ^{4}He [67]. In anisotropic antiferromagnets, the non-conserved components of the planar staggered magnetization ϕ_x and ϕ_y couple reversibly through the non-vanishing Poisson brackets to the conserved magnetization component M_z, resulting in the precession motion (4.5) of the spin vectors around a local field produced by their exchange interaction with their nearest neighbors and the external field.

One may view the conserved magnetization components acting as the infinitesimal rotation generators for the order parameter components, resulting in propagating spin waves in the ordered phase [11, 68]. The spin wave damping Γ_c decreases as the critical temperature is approached, with the associated relaxation time $\tau_{\rm rel} = 1/\Gamma_c$ diverging at T_c. Hence procuring the aging scaling data by probing the conventional two-time correlations turns out not to be a viable approach at the model F critical line. Moreover, owing to the reversible mode couplings between the conserved magnetization and the non-conserved order parameter components, the initial slip exponent θ and hence the autocorrelation exponent λ are expected to be non-universal in this case; specifically, these exponents should depend on the initial distribution of the magnitudes of the conserved modes [18, 30].

However, one can extract the dynamic exponent from the temporal evolution of the stationary correlation function in the vicinity of the critical parameters in the ordered phase. Near the critical temperature, the spin wave oscillations have an exponentially decreasing amplitude $\sim e^{-\Gamma_c t} \sim e^{-t/\tau_{\rm rel}}$. In a finite system near T_c, the stationary relaxation time diverges with linear system size with the dynamic critical

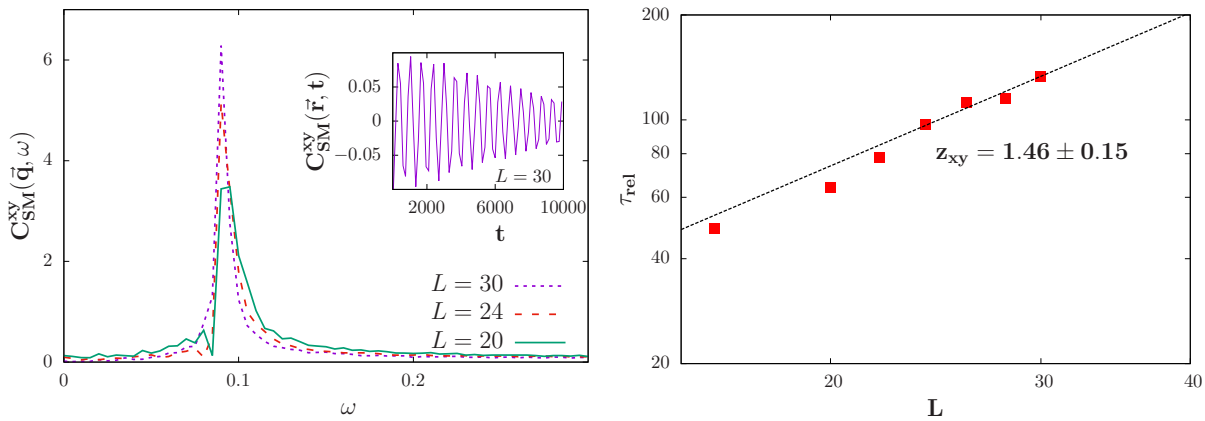

(a) (b)

Figure 4.6: (a) Fourier spectrum of the staggered magnetization correlation function in the xy plane for different linear system sizes $L = 20, 24, 30$ for a non-zero wave vector $\vec{q}$ vs. frequency ω. The inset shows propagating spin waves in the spin-spin correlation function with spatial separation $\vec{r}$ as a function of time. (b) Double-logarithmic plot of the relaxation time τ_{rel} vs. linear system sizes $L = 16 \ldots 32$. Fitting the data for large $L > 20$ yields the dynamic critical exponent $z = 1.46 \pm 0.15$.

exponent z characterizing its *critical slowing down*: $\tau_{\text{rel}} \sim L^z$. We have obtained the relaxation time via measuring the half-peak width Γ_c of the Fourier transform of the spin-spin correlation function [69], $C^{xy}_{\text{SM}}(\vec{q},\omega) = \int C^{xy}_{\text{SM}}(\vec{r},t)e^{i\omega t}dt$, see Fig. 4.6(a). The asymptotic value of the dynamic exponent for model F is known exactly from the dynamic renormalization group, $z_{xy} = d/2$ in $d \leq 4$ dimensions [19, 20]. From our relaxation time data as function linear system size, we find that for the five largest L the best fit line gives $z_{xy} \approx 1.46$, within our error bars in agreement with the theoretical predition 1.5, c.f. Fig. 4.6(b). As one would expect, with larger system sizes z_{xy} tends towards the asymptotic value.

4.5 Bicritical dynamical scaling

The two continuous phase transition lines described by models C and F meet at a *bicritical point* which is described by a different dynamical universality class. In their field-theoretical analysis, Folk, Holovatch, and Moser found that irrespective of whether the static behavior of the system is described by the Heisenberg or biconical

renormalization group fixed point, the parallel and perpendicular order parameter components scale similarly in time with dynamic critical exponents $z_z \sim z_{xy} \approx 2.003$ and $z_m \approx 1.542$ in the asymptotic limit [55]. However, strong non-asymptotic effects originating from the mode coupling terms in the vicinity of the bicritical point lead to very different crossover dynamical exponents which exhibit weak dynamical scaling.

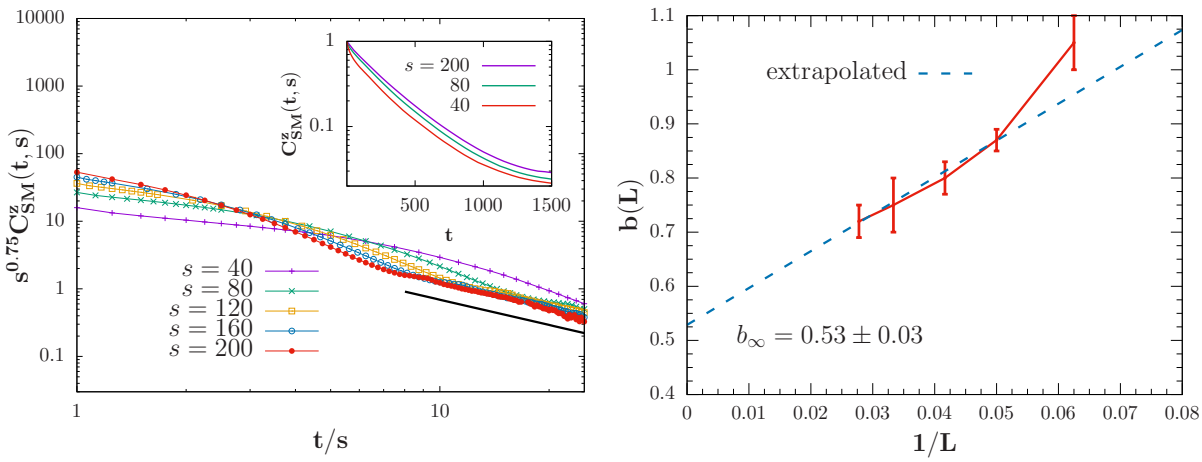

(a) (b)

Figure 4.7: (a) Aging scaling plots for two-time spin autocorrelation function $C^z_{\rm SM}(t,s)$ of the Ising antiferromagnetic order parameter on a simple cubic lattice of linear system size $L = 30$ with periodic boundary conditions. The system is quenched from an initially disordered configuration to the bicritical point at $T_c = 1.025$, $H^c_{\rm ext} = 3.825$. Double-logarithmic rescaled graphs for different waiting times s collapse with the scaling exponent $b \approx 0.75$. The inset shows the autocorrelation plots as a function of $t - s$, demonstrating broken time translation invariance. (b) Finite-size extrapolation analysis for the aging exponent b plotted vs. $1/L$ for five different linear system sizes $L = 16 \ldots 36$. A linear extrapolation using the data from the four largest systems to the infinite system size limit $L \to \infty$ yields $b_\infty = 0.53 \pm 0.03$.

Similar to the model C analysis, we obtain a dynamic aging scaling window for waiting times $s = 80 \ldots 200$ for the easy-axis scalar order parameter at the bicritical point. Figure 4.7 depicts the scaling collapse of the two-time autocorrelation plots for different waiting times for a system with linear size $L = 30$ with aging exponent $b \approx 0.75$. A subsequent system size extrapolation yields the asymptotic value $b_\infty = 0.53 \pm 0.03$. Using Eq. (4.9), one can then infer the dynamic critical exponent $z_z = 1.962 \pm 0.15$ which is in agreement with the theoretical prediction within our error bars. From the mean value of $\langle \lambda / z_z \rangle = 1.265 \pm 0.03$ over five different system sizes

(c.f. Fig. 4.8), we also obtain the bicritical initial slip exponent $\theta = 0.265 \pm 0.05$ for the staggered magnetization along the z axis.

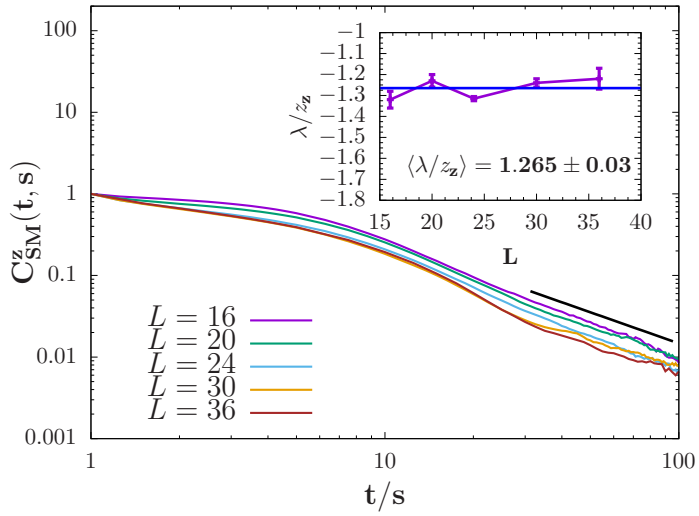

Figure 4.8: Double-logarithmic plots of the two-time staggered magnetization autocorrelation function vs. t/s for different linear system sizes L taken at an early waiting time $s = 40$ exhibit power law decays in the long-time limit $t \gg s$. The mean value of the autocorrelation exponent is determined to be $\langle\lambda/z_z\rangle = 1.265 \pm 0.03$.

4.6 Conclusion

We have utilized a hybrid numerical method that incorporates reversible spin precession dynamics through a deterministic integration scheme with relaxational Monte Carlo kinetics to investigate the both the stationary critical dynamics and the non-equilibrium critical relaxation in three-dimensional anisotropic antiferromagnets in an external magnetic field. From the aging scaling data of the order parameter spin autocorrelation function at the model C critical line, we obtained the aging and autocorrelation exponents. A systematic finite-size extrapolation analysis allowed for the extraction of the asymptotic value of the aging collapse exponent $b \approx 0.482$, which leads to the dynamic exponent $z_z \approx 2.148$. This is in very good agreement with the theoretical prediction. Further, we report the value of the initial slip exponent $\theta \approx 0.14$. Additionally, we extract the dynamic exponent for the conserved magnetization $z_m \approx 2.62$ and observe two distinct time scales in the decay of its two-time spin autocorrelation function.

In the vicinity of the model F critical line, the presence of spin waves hindered the aging scaling analysis. However, from the Fourier transform analysis of the spin waves we obtained the critical relaxation times that increase algebraically with system size, with the dynamic critical exponent $z_{xy} \approx 1.46$, which agrees with the theoretical value $z_{xy} = 3/2$ within our systematic and statistical errors. Finally, we performed an aging scaling analysis for the scalar order parameter component along the direction of the external field at the bicritical point. We thus verified that the dynamic exponent at this point $z_z \approx 1.962$ is different from the corresponding values at both the model C and model F critical lines, contrasting the nature of the dynamical universality class at the bicritical point.

4.7 Appendix

4.7.1 Equations of Motion for the Spin Vectors

The Hamiltonian of a three-dimensional antiferromagnet with anisotropic Heisenberg exchange interactions (with $J > 0$) in an external magnetic field is given by

$$\mathcal{H} = J \sum_{\langle ij \rangle}^{N} \left[\Delta (S_i^x S_j^x + S_i^y S_j^y) + S_i^z S_j^z \right] - H_{\text{ext}} \sum_{i=0}^{N} S_i^z \tag{4.12}$$

Using eqn. 3.14 one can write for the z-component,

$$\frac{dS_i^z}{dt} = J\Delta \Big(S_y^i \sum_j S_j^x - S_x^i \sum_j S_y^j \Big)$$

In terms of the variables ϑ and φ,

$$-\sin\vartheta_i \frac{d\vartheta_i}{dt} = J\Delta \Big[\sin\vartheta_i \sin\varphi_i \sum_j \sin\vartheta_j \cos\varphi_j - \sin\vartheta_i \cos\varphi_i \sum_j \sin\vartheta_j \sin\varphi_j \Big]$$

Thus we obtain,

$$\frac{d\vartheta_i}{dt} = -J\Delta \sum_j \sin\vartheta_j \sin(\varphi_i - \varphi_j) \ . \tag{4.13}$$

For the polar angle φ we solve the equation of motion for the x-component,

$$\frac{dS_x^i}{dt} = \cos\vartheta_i \cos\varphi_i \frac{d\vartheta_i}{dt} - \sin\vartheta_i \sin\varphi_i \frac{d\varphi_i}{dt}$$

Also, from eqn 3.14,

$$\begin{aligned}
\{S_x^i, \mathcal{H}\} &= J\Delta S_i^z \sum_j S_j^y - J S_i^y \sum_j S_z^j + H_{ext} S_i^y \\
&= J\Delta \cos\vartheta_i \sum_j \sin\vartheta_j \sin\varphi_j - J \sin\vartheta_i \sin\varphi_i \sum_j \cos\theta_j + H_{ext} \sin\vartheta_i \sin\varphi_i
\end{aligned}$$

Equating the above two equations,

$$\begin{aligned}
-\sin\vartheta_i \sin\varphi_i \frac{d\varphi_i}{dt} = J\Delta \cos\vartheta_i \cos\varphi_i \sum_j \sin\vartheta_j \sin(\varphi_i - \varphi_j) + J\Delta \cos\vartheta_i \\
\sum_j \sin\vartheta_j \sin\varphi_j - J \sin\vartheta_i \sin\varphi_i \sum_j \cos\theta_j + H_{ext} \sin\vartheta_i \sin\varphi_i \ .
\end{aligned}$$

$$\begin{aligned}
\implies \frac{d\varphi_i}{dt} = J \sum_j \cos\vartheta_j - H_{ext} - J\Delta \cot\vartheta_i \Big(\cot\varphi_i \sum_j \sin\vartheta_j \sin(\varphi_i - \varphi_j) \\
+ \frac{1}{\sin\varphi_i} \sum_j \sin\vartheta_j \sin\varphi_j \Big)
\end{aligned}$$

$$\begin{aligned}
= J \sum_j \cos\vartheta_j - H_{ext} - J\Delta \cot\vartheta_i \sum_j \sin\vartheta_j \\
\Big(\frac{\sin\varphi_j}{\sin\varphi_i} + \frac{\cos\varphi_i}{\sin\varphi_i} [\sin\varphi_i \cos\varphi_j - \cos\varphi_i \sin\varphi_j] \Big)
\end{aligned}$$

$$\begin{aligned}
&= J \sum_j \cos\vartheta_j - H_{ext} - J\Delta \cot\vartheta_i \sum_j \sin\vartheta_j \Big(\frac{\sin\varphi_j}{\sin\varphi_i} + \cos\varphi_i \cos\varphi_j - \cos^2\varphi_i \frac{\sin\varphi_j}{\sin\varphi_i} \Big) \\
&= J \sum_j \cos\vartheta_j - H_{ext} - J\Delta \cot\vartheta_i \sum_j \sin\vartheta_j \Big(\cos\varphi_i \cos\varphi_j + \sin\varphi_i \sin\varphi_j \Big)
\end{aligned}$$

$$\implies \frac{d\varphi_i}{dt} = J\sum_j \cos\vartheta_j - H_{ext} - J\Delta\cot\vartheta_i \sum_j \sin\vartheta_j \cos(\varphi_i - \varphi_j) \tag{4.14}$$

4.7.2 Hybrid Simulation Steps

In order to equilibriate the system at the temperature and the external field of the quench, the following steps are performed during simulation:

- Since only the z-component of the magnetization is conserved by the Hamiltonian as in section 4.2:
  1. Exchange the azimuthal angle ϑ with one of the six neighboring spins with probability 1/6.
  2. Rotate the polar angle φ with a random angle between 0 and 2π picked from a uniform distribution.
  3. Calculate the energy difference ΔE resulting from this update. Define the probability of update according to Glauber kinetics [59],
  $$W = \frac{1}{1 + \exp(\Delta E/k_B T)} \ .$$
  4. Generate a random number r from a uniform distribution between 0 and 1.
  5. If $r < W$, carry out the update. If not, restore the spins to previous configuration.
- In order to simulate the precession of the spin variables which result in reversible dynamics, integrate the equations of motion of the azimuthal and polar angles of the spins, Eqns. (4.13), (4.14) respectively at each lattice site.
- Update the lattice configuration with 10 sweeps of the Monte Carlo algorithm and then parallelly integrate all the spins by implementing 4th order Runge-Kutta algorithm. This combination is defined as one simulation time step (STS).

Chapter 5

Biological transport

Biological transport phenomena are of paramount importance for understanding the intricacies of how living organisms work. From the diffusion of molecules and nutrients across the cell and tissue membranes, the transfer of heat or mass along capillaries, the transport of organelles and vesicles by molecular motors inside the cells, the systematic functioning of all life is ensured by efficient transport mechanisms. These processes are fundamentally out of equilibrium as they either include active transport driven by external energy sources such as the hydrolysis of an ATP, or passive transport driven by concentration gradients.

In 1968, a very simple one-dimensional toy model, the totally asymmetric simple exclusion process (TASEP), was used for the first time to model the collective movement of ribosomes on a messenger RNA track [70]. Later, the asymmetric simple exclusion process (ASEP), a lattice-based model for a system of interacting particles, was introduced by Spitzer in 1970 [71], and since then has become a paradigmatic model for studying stochastic models of transport phenomena. In its most simple construct, the model consists of N particles hopping with probability p to the left and probability $q = (1-p)$ to the right on discrete lattice sites provided that the sites are empty. TASEP is a special case of the more general ASEP model, in which the probability p with which a particle moves to the left is one. The model also captures particle exclusion, where two particles are effectively considered hard spheres that cannot occupy the same sites. Due to its rich exhibition of multiple non-equilibrium stationary states that can be exactly obtained through rigorous mathematical analyses, the ASEP is an extensively studied non-equilibrium statistical model. Given that one can also add many realistic components to the simple model such as particle deposition and evaporation, multiple transport lanes, complex non-exponential wait times, and so on, the ASEP is still a very adequate framework for investigating transport phenomena.

5.1 Structure of part II

In the following chapter 6, we investigate the dynamics of a collection of molecular motors known as cytoplasmic dyneins by modeling them on a one-dimensional lattice as a variant of the TASEP model. We report the motor distributions, the density profile, and the stationary mean-field current after the system has reached its non-equilibrium stationary state (NESS). We also study the early time-dependent growth of the ensemble averaged mean square displacement that reveals the scale-invariant features of the model. A summary of this work is included in chapter 7 along with a brief outlook to the ongoing avenues that we are exploring in this research.

Chapter 6

Dynein-inspired one-dimensional exclusion process

This chapter is adapted from our publication, *Riya Nandi and Priyanka,"One-dimensional exclusion process with dynein inspired hops: simulation and mean field analysis", first published in J. Stat. Phys.* ***182****, 29 (2021) by Springer Nature. Reproduced with permission from Springer Nature.*

My contributions to this manuscript include developing the lattice simulation algorithm for the exclusion process, analysing the data, and preparing the first draft of the manuscript including the figures.

6.1 Introduction

Biological molecular motors are protein molecules that transport molecular cargo within the living cells by moving progressively along actin filaments and microtubules [72, 73]. The term "motor" is motivated by the fact that molecular motors utilize the chemical energy produced by the hydrolysis of ATP (Adenosine triphosphate) to ADP (Adenosine diphosphate) to perform mechanical work. This progressive movement of motors is often considered as analogous to the traffic in a city, where the cytoskeletal filaments act as the path along which the molecular motors travel in a directed fashion [74]. The efficient transport of molecular motors is critical for the healthy functioning of a cell as they play crucial roles in many biological processes such as cell division, transfer of genetic information, etc. Therefore, understanding the motor dynamics constitutes an important and relevant research area. Among the three known motor families, kinesins and dyneins move along a microtubule, whereas myosins move on an actin filament [75]. Unlike the other two, cytoplasmic dynein mediates retrograde transport shuttling organelles, vesicles, etc. from the edge to

the body of the cell. Owing to several experiments and theoretical modeling of the dynamics of motors in the last few years, we have a reasonably good understanding of the mechanism of processive backward/forward motion of kinesin and myosin. However, the functioning of cytoplasmic dynein is much less understood. Advancement in probing techniques in recent years has shed some light on the structural complexity and motility of dynein motors. Moreover, experimental studies of dynein have shown that they exhibit an unusual gear-like mechanism taking variable step sizes of 8, 16, 24, and 32 nm depending on the concentration of ATPs available and external loads [76, 77].

Motivated by this jump strategy with variable step-size, in this work, we introduce a simple one-dimensional stochastic model, with the goal to understand the effect of this motility mechanism on the collective dynein dynamics. Both analytical and numerical stochastic modeling of statistical physics is predominantly used to understand wide varieties of biological phenomena ranging from transport to cell division [78, 79, 80, 81]. For such studies, particle-based modeling [71] constitutes a simplified, idealized but powerful approach where one ignores the structural complexity of individual biological motors and considers them as hardcore particles that jump (move) across lattice sites (linear microtubule tracks). The process of hydrolysis is a constant source of energy to the motors, which can be represented in the model as a constant driving force for the particles. Such a driving force prevents the system from ever relaxing to thermal equilibrium. Thus, after an initial transient period of non-equilibrium dynamics, the system asymptotically evolves to a non-equilibrium stationary state [78]. Variants of the TASEP were introduced to study molecular motors [79]; however, very few of the earlier studies are based on dynein motors [82, 83, 84, 85]. An earlier study used a stochastic cellular automata model to represent the collective behavior of dynein motors [82]. However, this study did not incorporate the effect of load and hindrance together. To understand the dependence of the collective behavior of dynein motors on both load and blockage due to traffic, we formulate a TASEP variant. We specifically ask how dyneins optimize step sizes depending on parameters such as load and the presence of other motors [84, 86]. In this approximate model of dynein transport, which incorporates the essential load-dependent hopping mechanism, we investigate their long-time as well as the transient time behavior. Although open boundary conditions represent a more realistic model for a system of biological motors, we decide to study the system with periodic boundary conditions first since the bulk properties of the system are not affected by this choice. Later we look at the boundary effects by simulating our model with open boundary conditions. We find that the stationary-state gap distribution in front of the motors exhibits intriguing peaks at multiples of the maximum

jump size, with the amplitude of these peaks decaying exponentially as a function of the gap size. For open boundary conditions, we observe a damped oscillatory density profile starting from the entry sites. Depending on the influx and escape rates and the rates of attachment/detachment, these oscillations decay as one moves further into the bulk leading to a flat density profile. We also analyze the superdiffusive growth of the mean square displacement during the transient time followed by standard diffusive behavior.

Further, some experimental observations have revealed that under the effect of forces in the direction opposing the motion of the motors, they unbind from the tracks, thus decreasing their processivity [87, 88]. Inspired by the phenomena of "finite processivity", we perform simulations for the open boundary conditions with Langmuir kinetics [89]. In-vivo studies of dyneins, in particular, show that for low load, the probability of unbinding increases with load. However, at higher load, the dyneins exhibit catch-bond type behavior [90] which results in the probability of unbinding decreasing with increasing load. Here we want to emphasize that our goal is not to mimic the exact functional form of the load-dependence but to probe the effect of adding a non-zero probability of evaporation and deposition of particles on the steady-state distributions of our exclusion process as a mere exercise.

This paper is structured as follows: In the following section, we describe our stochastic model and review the known gear-like jump mechanism of dynein motors. We then discuss the results for the static and dynamics of the model for periodic boundary conditions in Section 6.3.1. Section 6.3.2 is devoted to the discussion of the properties of the model for open boundary conditions. Following that, we discuss the effects of adding Langmuir kinetics on the open boundary steady-state properties in Section 6.3.3. We conclude with a summary of our results and open questions in Sec. 6.4.

6.2 Model and Simulation Method

In this section, we briefly review the structure and the mechanism of motion of dynein motors; we refer the reader to Ref. [76] for a detailed description. Cytoplasmic dyneins perform unidirectional discrete jumps on the microtubule. A single microtubule consists of approximately 13 protofilaments, and it has been assumed that dynein uses more than one protofilament to walk due to its large structure [91, 92]. Structurally, a dynein motor has two heads; each head contains 6 AAA (ATPases Associated with diverse cellular Activities) domains, four of which are po-

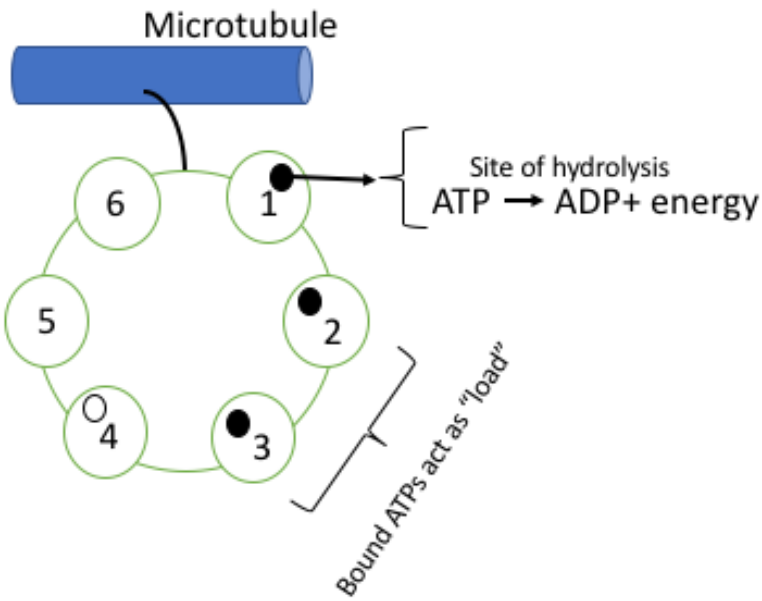

Figure 6.1: Schematic of a single head of dynein attached to the microtubule. Each head has six ATP binding sites (AAA1-6).

tentially ATP binding sites, as shown in Fig. 6.1. Earlier studies of dynein motors show that the hydrolysis (conversion of ATP to ADP) occurs on all ATP binding sites; however, only the hydrolysis at the primary site AAA1 is compulsory for the movement of the motors, so the motors do not hop until the primary site hydrolyzes. The attached ATP units on the secondary sites act as an external load for the motors, which determine the step size over the microtubule and also influence other molecular functions [77, 84]. In our study, we simplified the system by considering that dyneins with stacked head walk on a single protofilament, which has been also observed previously in certain in-vitro experiments [93] where they demonstrate that multiple rows of parallel protofilaments are not essential for the motility of the dyneins. In their Monte-Carlo studies, Mallik et al. [77], have also previously argued that considering the dynein as a single-headed structure is a reasonable assumption.

In our study, we introduce a variant of the totally asymmetric exclusion process to model the dynamics of dynein motors. We consider L discrete lattice sites with N hardcore particles which we refer to as N-motor system. A lattice site can be occupied by at most one particle, and each particle jumps in the forward direction with varying step sizes of 1, 2, 3 or 4 depending on the number of ATP units

attached to the secondary sites (loads) of the particle. Each particle carries a flag for the occupancy of one primary and three secondary ATP binding sites. Additionally, we also assume that there is an infinite source of ATP units available for binding. We employ random sequential Monte-Carlo update where, at each time step of the simulation, a motor is chosen randomly from an occupied lattice site. The hopping probability with varying step size is determined by three distinct processes:
ATP attachment- One unit of ATP attaches to the empty primary site with a constant probability P_{on} or to any of the available secondary sites, with a constant probability S_{on}.
ATP detachment- One unit of ATP detaches either from the primary or one of the three secondary sites with constant probabilities P_{off} and S_{off}, respectively.
ATP hydrolysis- A filled primary binding site hydrolyzes and converts ATP to ADP. This chemical reaction leads to energy production, which propels the motor forward. The number of steps the motor moves depends on the number of ATP units bound to the secondary sites and the number of available empty lattice sites in front of the motor. If the secondary ATP binding sites are unoccupied, the motor attempts to hop to the maximum step size of four. If s number of secondary sites hold ATP (s can be 1, 2, or 3), given the primary binding site is occupied, the motor attempts to hop $(4-s)$ steps. The motor can only take a step forward as long as there is no other motor blocking its path. If n is the attempted hopping size and m is the number of empty lattice sites in front of the motor, it takes $\min(m, n)$ steps. In actual biological motors, even the secondary sites hydrolyze ATP to ADP, but this does not result in forward-propulsion of the motor. In our N-motor system, secondary site hydrolysis is not considered. However, one can argue that the detachment rate of AAA(2-4) takes care of the hydrolysis of ATP from secondary sites.

The stochastic probabilities of attachment and detachment P_{on}, S_{on}, P_{off}, S_{off} are in general considered to be functions of the stall force, the temperature of the cellular environment and concentration of available ATP [77]. However, for this study, we choose constant probabilities. Based on some of the in-vitro experimental observations [94, 95] where the attachment rate of ATP to the primary site is large in comparison to the ATP attachment rate to secondary sites, we will present most of our results for high attachment rates to AAA1, specifically for the case when, $S_{on} = 1 - P_{on}$, $P_{off} = 1 - P_{on}$, $S_{off} = P_{on}$. All simulation results are obtained for lattice size $L = 10^3$ for periodic boundary conditions and $L = 500$ for open boundary conditions. Ensemble averaging of 10^4 different realizations have been performed for all final results.

For the maximal step size m_s, the rate of hopping n steps with m empty sites in

front of a particle is given by,

$$u_n(m) = \sum_{i=1}^{m_s-1} \delta_{n,i}[v_{2i-1}\delta_{m,i} + v_{2i}\theta(m-(i+1))] + v_{2m_s-1}\theta(m-m_s)\delta_{n,m_s} \ , \quad (6.1)$$

where the rates v_j are the constant rate of hopping which depend on the number of ATP molecules attached to the binding sites. v_{2n} denote the rate of jumping n steps if $m > n$ empty sites are in front of the particle and v_{2n-1} is the rate of jumping n steps if exactly n empty sites is in front of the particle. Also $\theta(x)$ is a discontinuous function whose value is zero for $x < 0$ and one for $x \geq 0$. The terms within the summation give the hopping rates for jump lengths smaller than m_s, and the last term denotes the hopping rate for maximum jump length, m_s.

In our model of dynein motors, where a motor can take maximum four steps ($m_s = 4$),

$$\begin{aligned} u_n(m) &= [v_1\delta_{m,1} + v_2\theta(m-2)]\delta_{n,1} + [v_3\delta_{m,2} + v_4\theta(m-3)]\delta_{n,2} \\ &\quad + [v_5\delta_{m,3} + v_6\theta(m-4)]\delta_{n,3} + v_7\delta_{n,4}\theta(m-4) \ , \end{aligned} \quad (6.2)$$

For $m_s = 4$, approximated functional form v_i in term of the attachment and detachment rate of ATPs' to the binding sites are given as,

$$\begin{aligned} v_7 &\approx P_{on}(1-P_{off})\left[\sum_{i=0}^{3}(S_{on}S_{off})^i(1-S_{on})^{3-i}\right] \ , \\ v_6 &\approx P_{on}(1-P_{off})S_{on}(1-S_{off})[(S_{on}S_{off})^2 + (1-S_{on})^2 + (1-S_{on})S_{on}S_{off}] \ , \\ v_5 &\approx v_7\rho + v_6 \ , \\ v_4 &\approx P_{on}(1-P_{off})S_{on}^2(1-S_{off})^2[(1-S_{on}) + S_{on}S_{off}] \ , \\ v_3 &\approx (v_7+v_6)\rho + v_4 \ , \\ v_2 &\approx P_{on}(1-P_{off})[S_{on}^3(1-S_{off})^3] \ , \\ v_1 &\approx (v_7+v_6+v_4)\rho + v_2 \ . \end{aligned}$$

We have also written down the exact form of all the rates for $m_s = 2$ in the Appendix equation (6.31). Here, we aim to understand the effect of various rates of attachment/detachment, and of the motor density on the fluctuations and stationary state properties of the system. We have studied the system for both periodic and open boundary conditions shown in Fig. 6.2. For open boundary conditions, the same dynamical rules of hopping apply in the bulk as for the periodic boundary case. Moreover, the open ends of the lattice are attached to a reservoir through

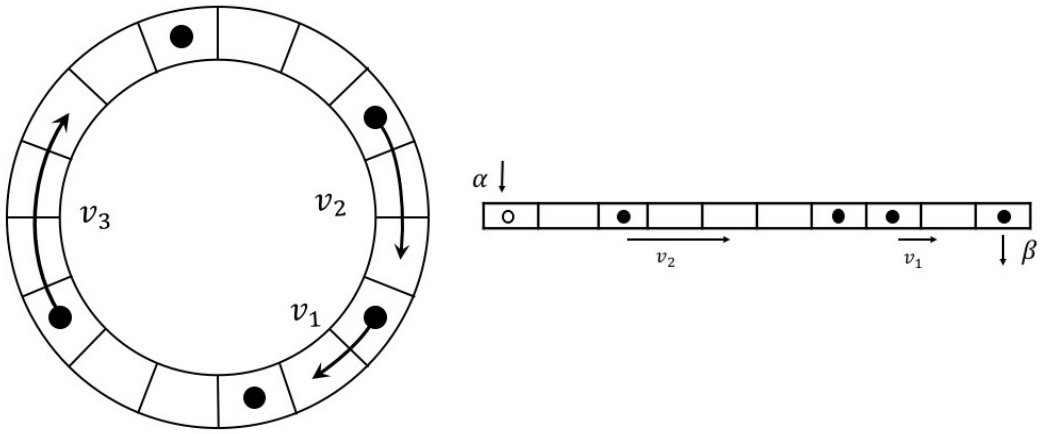

Figure 6.2: Transport of dynein motors on a lattice with periodic boundary conditions (left) and with open boundary conditions (right). For open boundary conditions, motors enter and exit the lattice with influx and escape rates α and β, respectively. Motors hop forward (clockwise) n steps with probability v_n and m ($m > n$) empty sites in front of them.

which a motor can enter and exit with the rates α and β from the first and last site, respectively.

6.3 Results

6.3.1 Periodic Boundary Conditions

Steady-state properties:

The system reaches its stationary state when the particle current does not change with time, which implies $\frac{dj}{dt} = 0$. we numerically calculate the time scale after which the particle current as well as the density profile become constant. In our model the steady-state is achieved by evolving the system for approximately L^2 Monte-Carlo steps. The stationary state current across the bond $i-1$ and i is the sum of all the

possible jumps and is given by

$$\begin{aligned} j(\rho) &= \langle v_1\eta_{i-1}(1-\eta_i)\eta_{i+1} + v_3\eta_{i-1}(1-\eta_i)(1-\eta_{i+1})\eta_{i+2} + ... + \\ &\quad v_2\eta_{i-1}(1-\eta_i)(1-\eta_{i+1})\sum_{l=0}^{\infty}\eta_{i+l+2}\prod_{k=1}^{l}(1-\eta_{i+1+k}) + ...\rangle \ , \end{aligned} \tag{6.3}$$

where η_j is occupancy of site j. We have also solved for the stationary state properties of the system in the mean-field approximation where we ignored all higher-order correlations, and for the two-point correlation, considered the factorization $\langle\eta_i\eta_j\rangle = \langle\eta_i\rangle\langle\eta_j\rangle = \rho^2$. This approximation manifests in two contexts the current work; one is to calculate the particle current and the other to calculate the mean-field gap distribution where we consider that the empty spaces are uncorrelated. One can define the mean-field particle current as

$$j(\rho) = \rho\sum_{i=1}^{m_s}\left[a_i\sum_{l=1}^{i}(1-\rho)^l\right] \ , \tag{6.4}$$

where, a_i is the probability of a particle to jump i steps and its value ranges between 0 and 1. For $m_s = 4$, $a_1 = v_1 + v_2,\ a_2 = v_3 + v_4,\ a_3 = v_5 + v_6$ and $a_4 = v_7$. Further for the limiting case of $P_{on} = S_{off} = 1,\ S_{on} = P_{off} = 0$, where the particles can take only four steps, the above expression for the current simplifies to,

$$j(\rho) = v_7\rho\sum_{i=1}^{4}(1-\rho)^i \ . \tag{6.5}$$

We then calculate the maxima of the current by setting $dj(\rho)/d\rho = 0$. For the limiting case, when $v_7 = 1$, the maximum current is obtained at density $\rho_{max} = 0.3312$. This is verified by our simulation result where the current profile for $P_{on} = 1$ indeed peaks at a $\rho \approx 0.33$ as can be seen from Fig. 6.3(a). We also observe that for all our chosen rates, the current reaches peak value at densities below $\rho = 0.5$. This shift of the peak below half-density signifies the absence of particle-hole symmetry. Simply put, in this system a particle moving four steps from site i to $i + 4$, is not equivalent to a hole moving from site $i + 4$ to i. This shift of maximum density below half also suggests the self-assembly of particles and holes to optimize the jump efficiency. To validate this claim, we investigate the flux due to "load" or ATP carried by the secondary sites, $L(\rho)$. For $P_{on} = 0.8$, $L(\rho)$ attains maximum value at $\rho \sim 0.4$ which is only slightly different from the density where density peak for the same choice of the rates, see inset of Fig. 6.3(a). Setting S_{on} equal to zero, and m_s to one, we

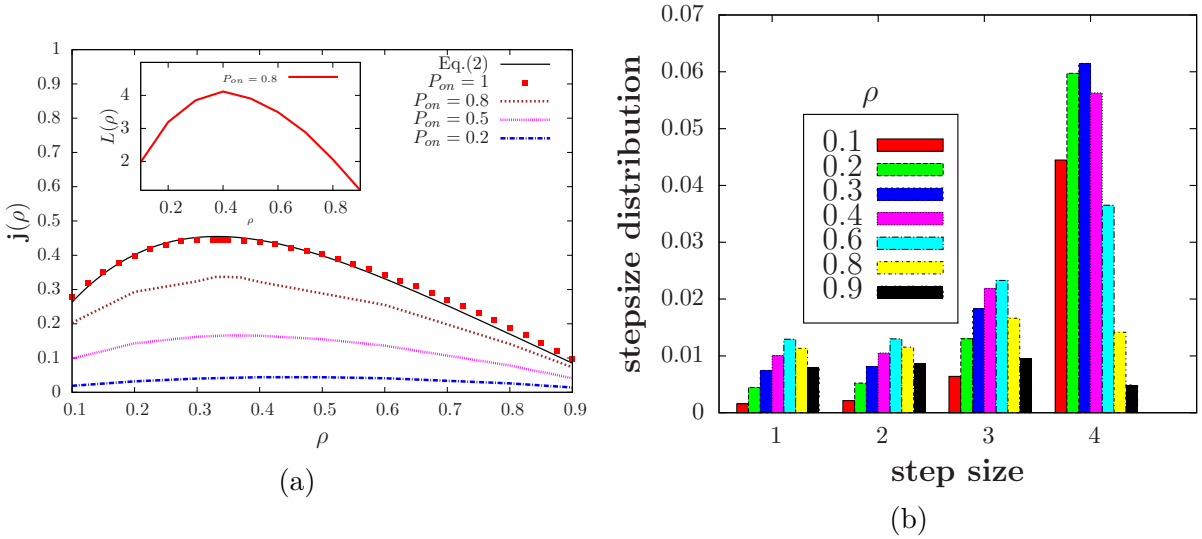

Figure 6.3: (a) Current profile $j(\rho)$ as a function of density for four different rates of attachment and detachment. The numerically obtained data points (red points) are compared with the mean-field Eq. 6.4 (black line) for $P_{on} = 1$, the maximum current is obtained at $\rho = 0.33$. The inset shows the flux due to "load" (ATP units carried by the secondary sites) $L(\rho)$, reaches maxima at density $\rho \sim 0.4$ for $P_{on} = 0.8$. (b) The distribution of the hop sizes performed by the motors in the stationary state peaks at hop size four for all densities. Attachment and detachment rates used in the simulation are $P_{on} = S_{off} = 0.8$, $P_{off} = S_{on} = 0.2$.

recover the well-known TASEP results [71].

In order to further investigate this self-organization of the particles, we probe into the distribution of particle clusters as well as the distribution of empty spaces in front of the particles referred to as *gap distribution*, $P(m)$. In the stationary state, the particle cluster is an exponentially decaying function for all choices of rates at all densities, as shown in Fig. 6.4(a). The characteristic size of the cluster depends not only on the density but also on the chosen rates of attachment and detachment. One can also extract the correlation length from the slopes for the log-linear plot of cluster distribution. The calculated correlation length is a measure of the size of the particles' clusters that are distributed over the entire lattice and we find that these clusters grow exponentially with density owing to the absence of long-range correlations. Moreover, the gap distribution shows a very striking feature for our specific choice of P_{on}, S_{on}, P_{off}, and S_{off}: The distribution peaks at multiples of the

maximum possible step size m_s, and the amplitude of the peaks decay exponentially, for all densities as can be seen in the inset of Fig. 6.4(b). The exponential decay of the distribution of the gaps with density is just complementary to the exponential growth of the correlation length. We inspected this further by simulating the gap distribution for various m_s, and the characteristic features of the peaks observed are consistent. These peaks signify that the motors assemble themselves in such a way that they optimize the utilization of energy by covering the maximum possible steps during each jump. The amplitude of these peaks at exact gap sizes which are multiples of m_s is reduced with an increase in S_{on} which increases load and consequently the probability of the motors jumping by smaller step sizes. Thus, these peaks can be attributed to the smaller attachment rate of secondary sites which favors the large step-size of m_s. This is also verified in figure 6.10 for various choices of probabilities. This observation is supported by the step-size distribution plot 6.3(b) as well, where one can see the particles indeed prefer to hop by the maximum length of four steps rather than taking shorter steps of one, two or three for all range of densities. We also notice that the step size distribution of four steps peaks at the density $\rho \approx 0.3$.

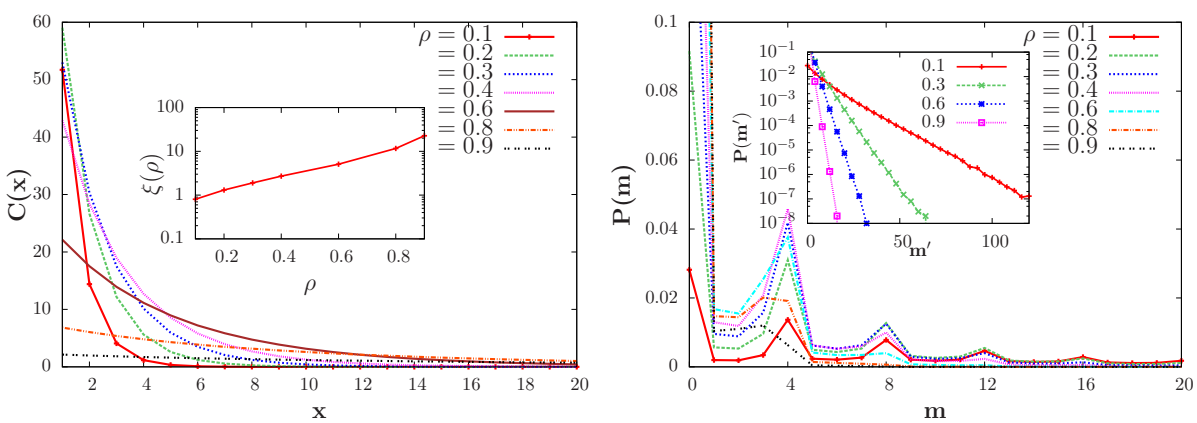

(a) (b)

Figure 6.4: (a)Particle cluster distribution $C(x)$ as a function of cluster size x for different densities show exponetial decay. Inset shows exponential growth of correlation length as a function of density. (b) The stationary-state gap distribution $P(m)$ shows peaks at multiples of four gap sizes for various densities. Inset shows the exponential decay of the distribution of the peaks $P(m')$ (here $m' = 4m$) for all densities. The rates of attachment and detachment here are $P_{on} = S_{off} = 0.8$, $P_{off} = S_{on} = 0.2$.

In order to analytically calculate the gap distribution, we assume that the system

has mean-field geometry where all the motors are connected to each other. In this limit, all the higher order correlations are ignored and the joint gap distribution $\mathcal{P}(m_1, m_2, m_3, ...m_n)$ of n particles having $m_1, m_2, ..m_n$ holes in front of them can be factorized i.e., $\mathcal{P}(m_1, m_2, ..., m_n) = \prod_i^n P(m_i)$. We write down the evolution equation for the probability of finding a gap of size m for a totally biased walk in the mean-field approximation as [82, 96, 97]:

$$\frac{dP(m,t)}{dt} = -\Big[\sum_{k=1}^{m} u_k(m) + \sum_{j=1}^{\infty} P(j,t) \sum_{k=1}^{j} u_k(j)\Big] P(m,t) + \sum_{k=1}^{m_s} P(m+k,t) u_k(m+k) + \sum_{k=1}^{m} P(m-k,t) \sum_{j=k}^{\infty} P(j,t) u_k(j) \qquad (m \geq 1) \ , \tag{6.6}$$

$$\frac{dP(0,t)}{dt} = -P(0,t) \sum_{j=1}^{\infty} P(j,t) \sum_{k=1}^{j} u_k(j) + \sum_{j=1}^{m_s} P(j,t) \sum_{k=1}^{j} u_k(j) \ . \tag{6.7}$$

The above equations must satisfy the following conservation rules,

$$\sum_{m \geq 0} P(m,t) = 1 \ , \tag{6.8}$$

$$\sum_{m \geq 1} m P(m,t) = \frac{1}{\rho} - 1 \ , \tag{6.9}$$

where $\rho = N/L$ is the density of motors present in the system. The conservation rules imply that we have a closed system with no global particle number fluctuations. To handle the infinite set of equations (6.7), we rewrite it into a single differential equation using the generating function technique where we multiply both sides of Eq. (6.7) by z^m, sum over all $m \geq 1$, and define the generating function $G(z,t) = \sum_{m \geq 1} z^m P(m,t)$. For the case of $m_s = 4$, the further calculation becomes cumbersome. Hence we carry out the analysis for a smaller step size $m_s = 2$ and arrive at the simplified form of the master equation in the stationary state. The detailed calculation and comparison of results with Monte Carlo simulations for maximum step size $m_s = 2$ are presented in Appendix 6.5. For any arbitrary jump size, the steady-state gap distribution has a polynomial solution and takes the following form for rate Eq. (6.1) [97]

$$P(m) = \sum_{i=1}^{m_s} \alpha_i q_i^m \ . \tag{6.10}$$

We can also define the current in terms of the gap distribution as

$$j(\rho) = \rho \sum_{k=1}^{m_s} P(k) \sum_{n=1}^{k} u_n(k) \ . \tag{6.11}$$

In addition to the static steady-state quantities, we also study the stationary state dynamical behavior by determining the mean square displacement of a tagged particle in this modified TASEP-like model. Earlier studies have shown that the variants of TASEP in one dimension fall in KPZ universality class, where dynamic exponent $z = 3/2$ [98, 99]. We calculate the stationary state mean square displacement of tagged particles defined as $\langle \delta\sigma^2(t) \rangle = \langle d^2 \rangle - \langle d \rangle^2$, where d is the average displacement traveled by the tagged particle and the angular bracket is an average over the different realizations starting from the same initial conditions for this N-motors system. Our simulation results show the same characteristic features as observed in the case of 1D TASEP [98]. We see the initial KPZ growth with an exponent 2/3 which is a signature of the TASEP universality class, followed by diffusion. The standard finite-size scaling form shows perfect scaling collapse with dynamical exponent $z_s = 3/2$, as shown in Fig. 6.5(a).

Transient behavior:

Next, we investigate the dynamics of the system starting with random initial configurations and calculate the mean square displacement of the motors in time,

$$\langle \delta r^2(t) \rangle = \langle r^2 \rangle - \langle r \rangle^2 \ , \tag{6.12}$$

where $r(t) = \dfrac{1}{N} \sum_{i=1}^{N} x(t)$ is the average displacement of the motors over the entire lattice and the angular bracket represents ensemble averaging.

We measure the mean square displacement for various densities as well as for different attachment and detachment rates. They all display power-law behavior with time $\langle \delta r^2(t) \rangle \sim t^{\gamma}$ as shown in Fig. 6.5(b). After a small initial time window $t_{mic} \sim 100$ time steps, the intermediate time growth of mean square displacement shows anomalous diffusion, which means faster than diffusive behavior. The best fit of the transient regime gives growth exponent $\gamma \approx 1.338 \pm 0.01$ before it crosses over to a standard diffusive regime at later times where γ is one. We also observe that the crossover time depends on the density of the motors present in the system. This

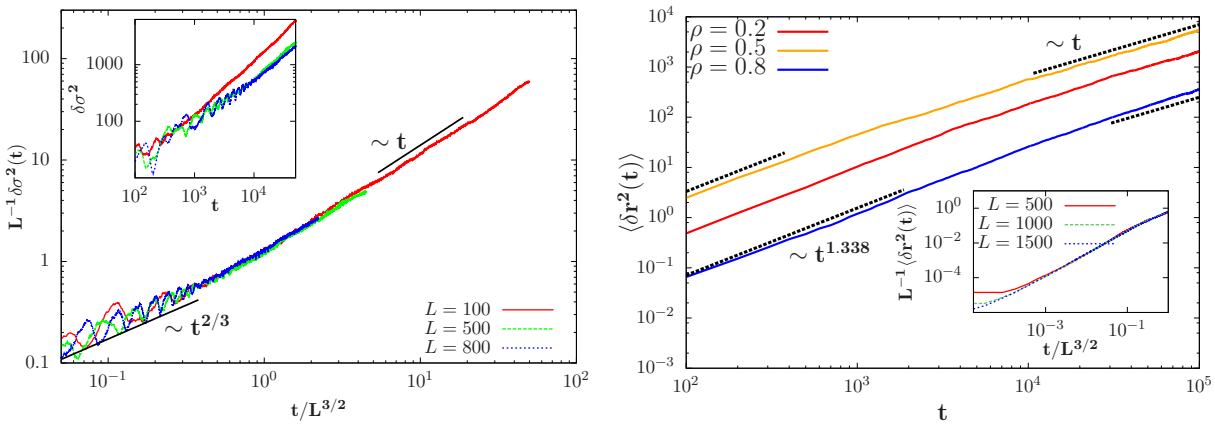

Figure 6.5: (a) Growth of the mean square displacement for a tagged particle with time in the stationary state. (b) Superdiffusive growth of the mean square displacement with time starting from a random initial condition at early times. Inset shows system size scaling with exponent $z = 3/2$. Rates of attachment and detachment chosen here are, $P_{on} = S_{off} = 0.8$, $P_{off} = S_{on} = 0.2$.

kind of super-diffusive behavior has been observed experimentally in the dynamical regime of molecular motors and other active cellular matter [100, 101, 102]. In most biological systems, short-range fluctuations are responsible for the diffusive propagation, whereas long-range fluctuations arising from directed transport driven by chemical energy cause super-diffusive dynamics [103, 104]. One can interpret the crossover from super-diffusive to diffusive behavior in our simulations with a similar argument. At early times, the motion is primarily dictated by individual hops resulting from ATP hydrolysis and uncorrelated collective dynamics. This weak super-diffusive power-law could perhaps also be attributed to logarithmic correction. After the transient period, the dominant stochastic collisions between the particles slow down the growth of mean square displacement, which results in standard diffusive behavior in the long-time regime. We also evaluate the dynamic scaling exponent using the finite-size scaling relation,

$$\langle \delta r^2(t) \rangle \propto L^{\xi} f\Big(\frac{t}{L^z}\Big). \tag{6.13}$$

The best data collapse gives the exponents $\xi = 1$ and $z = 3/2$, as shown in the inset of Fig. 6.5(b)).

6.3.2 Open Boundary Conditions

In this section, we discuss the results and analysis of the collective behavior of an N-motor system with open boundary conditions. The open boundary lattice is a more realistic depiction of the biological system as microtubules are open-ended tracks on which a motor can enter and exit from the left end (head) and the right end (tail), respectively. A motor enters with probability α provided that the first site is empty and exits from last lattice site with probability β. The rules of hopping in bulk are the same as in the periodic boundary case. However, if the particle reaches the last lattice site while hopping with the ATP dependent jump probability, then it exits the lattice. We perform simulations with three different rates of influx and escape: $\alpha = 2\beta$, $\alpha = \beta$, and $\alpha = \beta/2$, starting with different initial densities. For arbitrary m_s, one can write the per-site occupancy dynamics for density at the kth site ρ_k as

$$\frac{d\rho_1}{dt} = \alpha(1-\rho_1) - v_s\rho_1(1-\rho_2) \ , \tag{6.14}$$

$$\frac{d\rho_k}{dt} = \Big[\bar{v}\rho_{k-1} + \tilde{v}\rho_{k-2}(1-\rho_{k-1})\Theta(k-1)\Big](1-\rho_k)\rho_{k+1} + \sum_{j=1}^{\min(k-1,m_s)} v_j\rho_{k-j}\prod_{i=0}^{j-1}(1-\rho_{k-i}) - v_s\rho_k(1-\rho_{k+1}) \ , \qquad 1 < k < L \tag{6.15}$$

$$\frac{d\rho_L}{dt} = \sum_{j=1}^{m_s} v_j\rho_{L-j}\prod_{i=0}^{j-1}(1-\rho_{L-i}) - \beta\rho_L \ , \tag{6.16}$$

where $v_s = \sum_{j=1}^{m_s} v_j$, $\bar{v} = v_2 + v_3 + v_4$, $\tilde{v} = v_3 + v_4$, and α, β are the entry and exit rates, respectively.

Steady state properties:

We first analyze the stationary state density profile over the lattice. Interestingly, as can be seen in Fig. 6.6, we observe oscillatory behavior near the boundary, where the particles enter the system. The average density peaks at those lattice sites which are multiples of the maximum jump size m_s, with the amplitude of the peaks decaying exponentially as one moves further into the bulk. The characteristic decay length depends on the influx rate; the larger α, the faster the decay. The depth of these oscillations into the bulk of the system also decreases with the increasing influx rates, see 6.6(a). Significantly high influx rate causes crowding near the entry site forcing

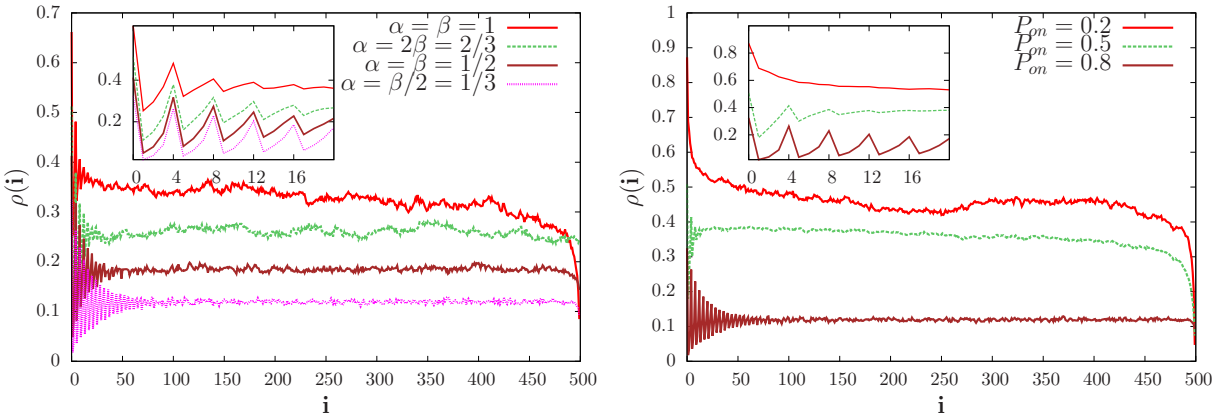

(a) (b)

Figure 6.6: (a) Stationary state density profile across the lattice sites for different influx and escape rates α and β, for $P_{on} = S_{off} = 0.8$, $P_{off} = S_{on} = 0.2$. The inset shows oscillations with periodicity of $m_s = 4$ in the density profile near the boundary through which the motors enter the system. (b) The density profile for different rates of attachment/detachment for $\alpha = 2\beta = 2/3$ shows similar periodic behavior near the entrance boundary.

the motors to take smaller steps. The depth of oscillations into the bulk also decreases upon lowering P_{on}, as shown in Fig. 6.6(b). Reducing P_{on} implies an increase in the attachment rate S_{on} of secondary ATP binding sites, which consequently increases the probability of taking smaller step sizes. Thus the amplitude of these oscillations decays and vanishes faster displaying a TASEP-like tangent profile [105]. From our simulation results, we conclude that the mean density in bulk never exceeds $\rho = 0.5$, even for significantly high influx rates. For large P_{on} and small S_{on} values, the bulk density profile is almost flat. The gap distribution shows similar peaks at multiples of the maximum step-size with exponentially decaying amplitudes as discussed for the case of periodic boundary conditions, see Fig. 6.7(a).

Transient behavior:

To understand the dynamics of the system, we furthermore analyze the mean square displacement $\langle \delta r^2(t) \rangle$ during the transient regime, as was done for periodic boundary conditions in sec. 6.3.1. During the growth of the mean square displacement, we observe three different growth regimes; the initial time dynamic exhibits a combi-

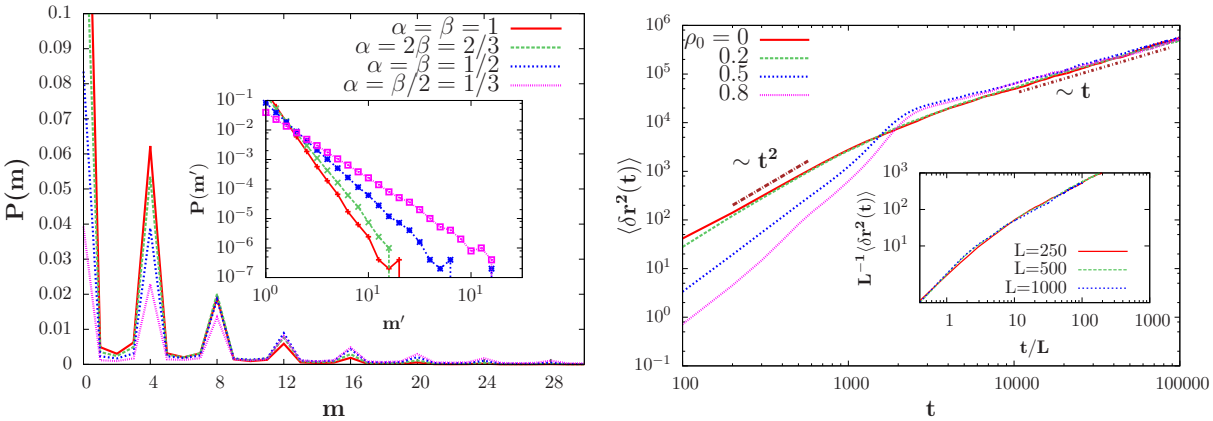

(a) (b)

Figure 6.7: (a)The stationary state gap distribution $P(m)$ shows peaks at multiples of 4 for different rates α and β, and the inset shows the exponential decay of these peaks with gap size m. (b) Growth of fluctuations for different starting densities, for the case $\alpha = 2\beta = 2/3$. The inset shows the finite size scaling collapse of mean square displacement with the dynamical exponent, $z = 1$.

nation of super-diffusive and ballistic growth ($\langle \delta r^2(t) \rangle \sim \Gamma t^{1.2} + \Gamma' t^2$, where Γ and Γ' are fitting parameters), followed by the complete ballistic growth ($\langle \delta r^2(t) \rangle \sim t^2$) in the intermediate regime. The long-time behavior of the system is predominantly diffusive. This ballistic growth preceding the diffusive stationary state can be explained by the accelerated motion of the particles in the intermediate regime as there is enough empty space present in front of them. We also probe the effect of different starting densities on the growth of fluctuations. As shown in Fig. 6.7(b), for zero initial density one observes a more prolonged ballistic regime; with the increase in initial density, the pure ballistic regime becomes negligible. For finite initial density, we observe prolonged mixed ballistic and diffusive dynamics. However, in the long-time regime, the dynamic behavior is independent of the initial densities, and the effect of stochastic forces start to become evident, forcing the motors to undergo diffusion [106, 107]. Furthermore, plots for different system sizes collapse according to the finite-size scaling relation (6.13) with exponents $\xi = 1$ and $z = 1$, as shown in the inset of Fig. 6.7(b)). The dynamical exponent $z = 1$ is the resultant of ballistic growth of fluctuations.

6.3.3 Effect of Langmuir Kinetics

Hitherto our analysis was based on the assumption that dynein motors do not unbind from the microtubule track; in other words, they exhibit "infinite processivity". But experiments have shown that molecular motors often unbind from the tracks with a load-dependent probability [87, 88]. Loose motors can also bind to the microtubule with a constant probability. The unbinding of motors from the filaments under load has been explored via various theoretical frameworks [108, 109]. In the present study, we analyze the effect of unbinding on the collective dynamics of the dyneins by introducing a load-dependent probability of evaporation P_{ev}. Since in our model the load is represented by the number of ATP molecules attached to the secondary sites, we model the probability of evaporation to be an exponential function $P_{ev} = \frac{e^{s-3}}{L}$, where $s = (0, 1, 2, 3)$ represents the number of ATPs bound to the secondary site [110] and L is the lattice size, a prefactor chosen to maintain the evaporation at a low threshold. We choose the constant probability of deposition such that it is equal to the lowest evaporation probability, $P_{dep} = \frac{e^{-3}}{L}$.

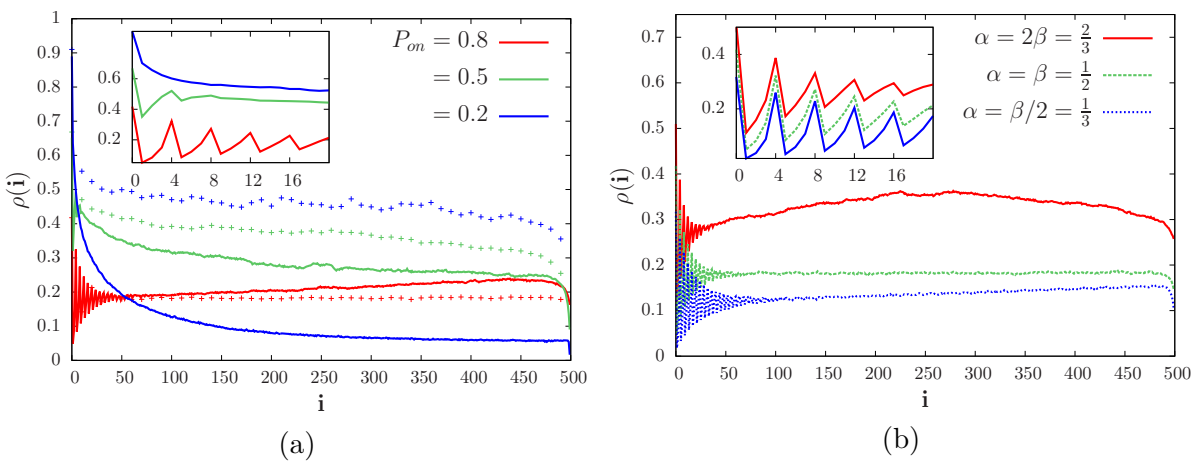

Figure 6.8: (a) Open boundary stationary state density profile for different rates of attachment/detachment. The solid lines represent data with Langmuir kinetics and the discrete points represent the corresponding data without Langmuir kinetics. The inset shows oscillations with periodicity four near the entrance boundary. The chosen probabilities of influx and escape are $\alpha = \beta = 0.5$. (b) Density profile for different probabilities of influx and escape for the probability of attachment/detachment $P_{on} = S_{off} = 0.8$, $S_{on} = P_{off} = 0.2$.

Comparing Fig. 6.8 to Fig. 6.6, we notice that the damped oscillatory behavior at

the entrance boundary remains unaffected by the addition of the Langmuir kinetics. From Fig. 6.8(a), it is important to note that the data corresponding to high load ($P_{on} = 0.2$) without Langmuir dynamics behaves almost like TASEP and hence the system is in the maximal current phase saturating at half density. Interestingly, adding Langmuir dynamics shifts the phase curve towards low density and it saturates at a much lower value of ~ 0.05. For low load conditions, $P_{on} = 0.8$, the effect of deposition of particles dominate near the rear boundary of the lattice, leading to a positive slope in the density profile. This slight positive slope in the bulk density is consistently observed for all the three cases of influx and escape rates, see Fig. 6.8(b). For the case with $\alpha = 2\beta = 2/3$, we observe that the density forms a cusp halfway through the lattice. We believe that this is an artifact of the competition between Langmuir dynamics and influx/escape dynamics. Even without the Langmuir dynamics, for lower escape rates β, the particle spends longer time on the lattice and hence they accumulate near the right boundary as seen in Fig 6.6(b). Further, we hypothesize that adding evaporation balances this accumulation on the right boundary leading to the cusp formation. However, a detailed analytical study is required to understand this behavior which is beyond the scope of the current work. Analogous to the results in the previous section without Langmuir kinetics, the gap distribution loses its multiple peak structure for high load, $P_{on} = 0.5$ and 0.2 as a result of both higher load forcing the particles to take smaller steps and random deposition of particles destroying the gaps of four as can be seen from Fig. 6.9(a). The gap distribution remains effectively unchanged for the various rates of influx α and escape β with the addition of deposition and evaporation, see Fig. 6.9(b).

6.4 Conclusion and Outlook

Our stochastic modeling of dynein motor transport on a lattice with the incorporation of varying hop sizes manifested many exciting results which include the oscillatory behavior of the "gap distribution" as well as the average density for the open boundary conditions, and superdiffusive growth of the fluctuations. Before probing into the combined effect of obstruction due to the presence of other motors and the impact of loads, we verified the experimental data for a single dynein motor given in the paper by Rai et al. [86] in our model. We found that without the traffic obstruction, a single dynein motor takes maximum jumps of step size = 4. We also verified that the motor increasingly takes smaller steps and the velocity exponentially decreases with increasing load. Moreover, including the crowded track along with the load in

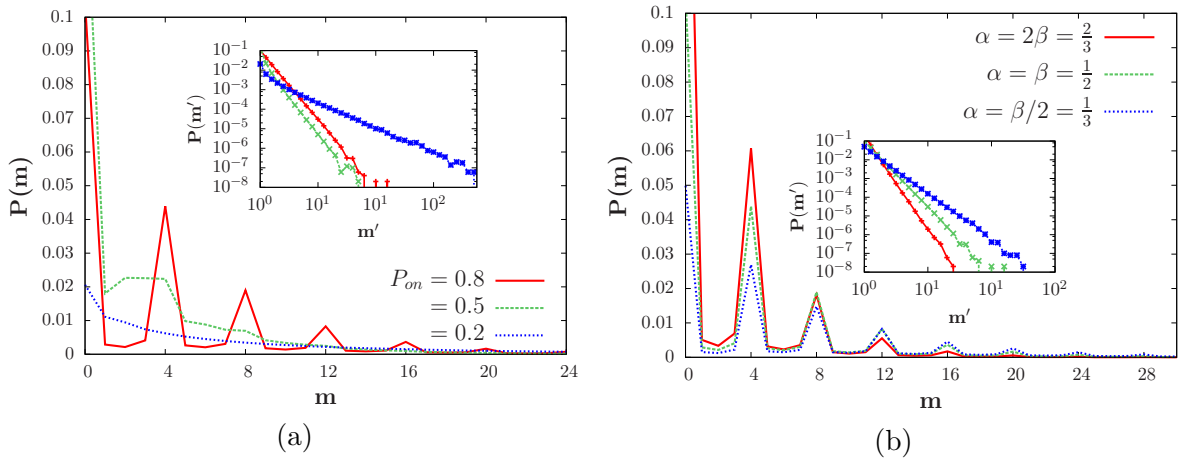

Figure 6.9: (a) Gap distribution for different rates of attachment/detachment with evaporation and deposition. The gaps peak at multiples of 4 for $P_{on} = 0.8$ which corresponds to low load. For high-load conditions the curve decays smoothly. Inset shows exponentially decaying amplitudes of the peaks. The chosen probabilities of influx and escape are $\alpha = \beta = 0.5$. (b) Gap distribution for different rates of influx and escape remain unaffected with the addition of deposition and evaporation. Chosen rates of attachment/detachment are $P_{on} = S_{off} = 0.8, P_{off} = S_{on} = 0.2$.

our model, we observe the distribution of step sizes. For low load attachment case, the effect of the hindrance due to the presence of other motors is not that prominent, and motors still on average prefer to jump four steps. Further, the stationary state current shows a breakdown of particle-hole symmetry and in the system exhibits free flow motion for densities smaller than ≈ 0.33, depending on the choice of attachment and detachment probabilities. The intuitive features of the gap distribution allowed us to obtain a better insight into the collective behavior and self-organizing nature of the dyneins for both open and periodic boundary conditions. The gap distribution peaks at gap sizes, which are multiples of the maximum step size, signifying that the motors organize themselves so they can jump by the maximum step size possible. We also carried out a mean-field calculation for the gap distribution.

For the more realistic scenario of open boundary conditions, our simulations capture a damped oscillating behavior of the density profile. The decay length highly depends on the attachment and detachment probabilities, as well as the influx and escape rates of the motors. Similar oscillations, albeit undamped unlike in our model, have been observed in earlier studies of dynein motors [82] using cellular automata;

here, we would like to emphasize the fact that different modeling approaches lead to very different results. The exact cause of this difference is an open question. For the simulations with Langmuir kinetics, the damped oscillations in the density profile and the discrete peaks in the gap distribution remained intact for low-load conditions. However, for high load, the distributions became smoother and imitated the results of TASEP. For the mean square displacement, we observe two regimes, an early time of fast growth followed by diffusive growth as the system approaches the stationary state. In the initial transient period, open and periodic boundary conditions show ballistic and superdiffusive growth with exponents 2 and 1.3, respectively.

In the future, we would like to expand our minimalistic model by adding complexities that depict more experimentally relevant and realistic scenarios. A few possible adaptations can be limiting the amount of available ATP, probing the dynamics of walking on multiple protofilaments, etc. It would also be interesting to test these results in an in-vitro experimental set-up of an assembly of dynein motors. Although one of the major challenges for such an experimental study is controlling the number of motors and maintaining the composition of the motor assemblies, experiments using biosynthetic methods on DNA scaffolds [111, 112, 113] have been conducted to investigate collective transport of motors. Our theoretical results illustrate how a group of dynein motors might be distributed on a single track depending on the load they carry, what would be the optimal density for them to most efficiently transport cargo and avoid over-crowding and thus, provide a significant point of reference for experiments on the collective motion of dyneins.

6.5 Appendix : Mean-field analysis of gap distribution

We analytically solve for the gap distribution P(m) for the case when a motor can hop to maximally 2 empty sites in front of it. The rate of hopping n steps with m empty spaces in front of the motor is,

$$\alpha_m(n) = (v_1\delta_{m,1} + v_2)\delta_{n,1} + v_3\delta_{n,2} + \theta(m-2)(v_2\delta_{n,1} + v_3\delta_{n,2}) \ . \tag{6.17}$$

The master equations for the time dependent gap distribution $P(m,t)$ are,

$$\begin{aligned}\frac{dP(0,t)}{dt} &= -P(0,t)\Big[v_1P(1,t)+(v_2+v_3)\sum_{m=2}^{\infty}P(m,t)\Big] \\ &\quad +v_1P(1,t)+v_3P(2,t)\ , \qquad (6.18)\\ \frac{dP(1,t)}{dt} &= -P(1,t)\Big[v_1(1+P(1,t))+(v_2+v_3)\sum_{m=2}^{\infty}P(m,t)\Big]+v_2P(2,t) \\ &\quad +v_3P(3,t)+v_1P(1,t)P(0,t)+v_2\sum_{m=2}^{\infty}P(m,t)P(0,t)\ , \qquad (6.19)\end{aligned}$$

$$\begin{aligned}\frac{dP(m,t)}{dt} &= -P(m,t)(v_2+v_3)-P(m,t)[v_1P(1,t)+(v_2+v_3)\sum_{m=2}^{\infty}P(m,t)] \\ &\quad +v_2P(m+1,t)+v_3P(m+2,t)+P(m-1,t)[v_1P(1,t) \\ &\quad +v_2\sum_{m=2}^{\infty}P(m,t)]+v_3P(m-2)\sum_{m=2}^{\infty}P(m,t)\ . \qquad (6.20)\end{aligned}$$

Since the total probability is conserved, $\sum_{m=0}^{\infty}P(m,t)=1$, defining $\sum_{m=k}^{\infty}P(m,t)=S_k$ and using the conservation law $P(0,t)+\sum_{m=1}^{\infty}P(m,t)=1$, we have

$$P(0,t)=1-S_1\ . \qquad (6.21)$$

Similarly, $P(1,t)$ can be represented as S_1-S_2. Using these substitutions, we arrive at the simplified form of the evolution equation,

$$\begin{aligned}\frac{dP(0,t)}{dt} &= -P(0,t)\Big[v_1P(1,t)+(v_2+v_3)S_2\Big]+v_1P(1,t)+v_3P(2,t)\ , \qquad (6.22)\\ \frac{dP(1,t)}{dt} &= -P(1,t)\Big[v_1(1+S_1-S_2)+(v_2+v_3)S_2\Big] \\ &\quad +v_2P(2,t)+v_3P(3,t)+\Big[v_1(S_1-S_2)+v_2S_2\Big]P(0,t)\ , \qquad (6.23)\\ \frac{dP(m,t)}{dt} &= -P(m,t)\Big[(v_2+v_3)(1+S_2)+v_1(S_1-S_2)\Big]+v_2P(m+1,t) \\ &\quad +v_3P(m+2,t)+v_3S_2P(m-2,t) \\ &\quad +P(m-1)[v_1(S_1-S_2)+v_2S_2] \qquad m\geq 2. \qquad (6.24)\end{aligned}$$

Defining the generating function, $G = \sum_{m=1}^{\infty} z^m P(m,t)$, we can write the evolution equation as,

$$\begin{aligned}
\frac{dG}{dt} &= \frac{d}{dt}\sum_{m=1}^{\infty} z^m P(m,t) \\
&= \Big[[(1+S_2)(v_2+v_3)+v_1(S_1-S_2)] + w_2 z^{-1} + w_3 z^{-2} \\
&\quad +[v_1(S_1-S_2)+w_2S_2]z + w_2S_2z^2\Big]G + z(v_2+v_3-v_1)P(1,t) \\
&\quad +v_2P(1,t) - w_3z^{-1}P(1,t) - v_3P(2,t) \\
&\quad +[v_1(S_1-S_2)+w_2S_2]zP(0,t)\ . \qquad (6.25)
\end{aligned}$$

In the stationary state, the probabilities are time independent. Hence, setting $\frac{dP(0,t)}{dt}$ equal to zero, one can obtain,

$$v_3P(2) = -v_1P(1) + P(m)[v_1P(1) + (v_2+v_3)S_2]\ . \qquad (6.26)$$

To solve for stationary state, we set $\frac{dG}{dt} = 0$, and plug Eq. (6.26) in Eq. (6.25) which gives us the following polynomial equation,

$$\begin{aligned}
&\Big[-z^4v_3S_2 - z^3[v_1(S_1-S_2)+v_2S_2] + z^2[(1+S_2)(v_2+v_3)+v_1(S_1-S_2)] \\
&-v_2z - v_3\Big]G = z^4v_3S_2(1-S_1) + z^3\Big[(v_2+v_3-v_1S_1)(S_1-S_2)v_2S_2(1-S_2)\Big] \\
&-z^2\Big[[v_1(S_1-S_2)+(v_2+v_3)S_2](1-S_1) + (v_1-v_2)(S_1-S_2) - v_3(S_1-S_2)z\ . \qquad (6.27)
\end{aligned}$$

Simplifying the above equation by taking out the common factor of $(z-1)$, we get

$$\begin{aligned}
&\Big[-z^3v_3S_2 - z^2[(v_2+v_3)S_2 + v_1(S_1-S_2)] + z(v_2+v_3) + v_3\Big]G = \\
&z^3v_3S_2(1-S_1) + z^2[(v_2+v_3)S_1(1-S_2) - v_1S_1(S_1-S_2)] + zv_3(S_1-S_2)\ . \qquad (6.28)
\end{aligned}$$

Further, we expand G, equate all coefficients for z^m from both sides of (6.28), and obtain the recursion relation for $P(m)$ which is also calculated in [97]. In case of

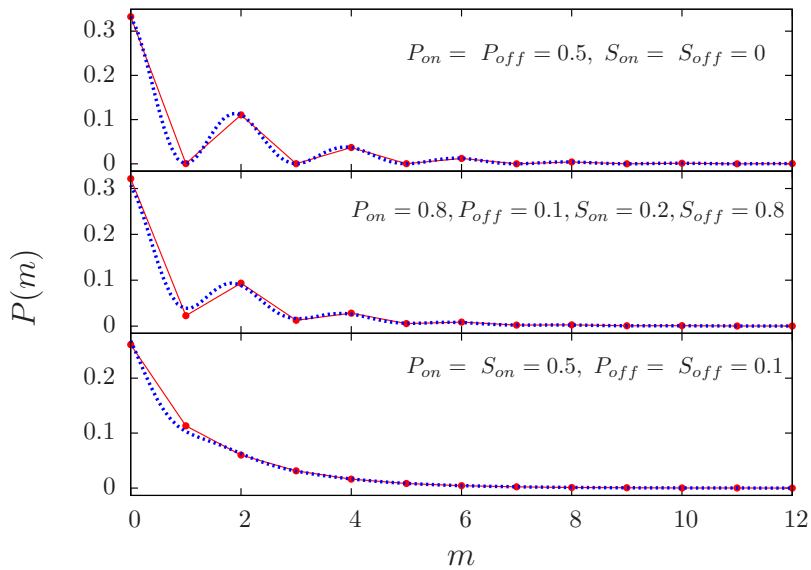

Figure 6.10: The gap size distribution for $m_s = 2$ for various probabilities of attachment and detachment. The analytical result (6.30) represented by dashed lines matches very well with our simulation results (line-point).

$m_s = 2$, the recurrence relation for $P(m)$ is given as

$$P(m)v_3 + P(m-1)(v_2+v_3) - P(m-2)(S_1v_1 - S_2(v_2+v_3-v_1)) \\ -P(m-3)S_2v_3 = 0\ . \tag{6.29}$$

Assuming a polynomial solution, $P(m)\ x^m$ and using in (6.29), we get a third order polynomial in x,

$$v_3x^3 + (v_2+v_3)x^2 - (S_2(v_2+v_3-v_1) + S_1v_1)x - S_2v_3 = 0\ . \tag{6.30}$$

Solution of above equation has three roots x_1, x_2, x_3 and hence $P(m) = c_1x_1^m + c_2x_2^m + c_3x_3^m$. Using conservation laws Eqs. (6.8) and (6.9), we consider that the coefficients $c_3 = 0$ and c_1, c_2 values depend on the rates. We solve two consecutive equations for specifying the values of the transition rates, v_1, v_2, v_3 and the density the ρ and solved for all the unknowns. We have shown the comparison of the solution with Monte-Carlo simulation of N-motor system in Fig. 6.10. v_i depends on the attachment and

detachment rates as,

$$\begin{aligned} v_2 &= P_{on}(1-P_{off})S_{on}(1-S_{off}) \ , \\ v_3 &= P_{on}(1-P_{off})((1-S_{on}) + S_{on}S_{off} \ , \\ v_1 &= v_3\rho + v_2 \ . \end{aligned} \tag{6.31}$$

Chapter 7

Summary and Outlook

In this dissertation, I studied two distinct non-equilibrium processes: critical aging scaling relaxation of three-dimensional antiferromagnets and dynein-inspired non-equilibrium transport phenomena in one-dimensional exclusion processes.

In chapter 2, I introduced the theoretical constructs of dynamical critical phenomena, reviewing the existing literature. I briefly reviewed Landau's phenomenological theory that leads to the derivation of the mean-free critical exponents. This theory sets the foundations on which the concept of universality and scaling hypothesis is based and we presented the equations describing the static and dynamic scaling of the variables that exhibit singularity at the critical point. Following this, I moved on to the next logical step in this formulation that includes the effects of the stochastic spatial fluctuations, the Landau-Ginzburg-Wilson Hamiltonian. I then discussed the Langevin equations characterizing the different dynamic universality classes. Finally, I introduced the theory of aging scaling, a non-equilibrium relaxation regime observed in the early times after a system is suddenly quenched from an initially disordered state to an ordered state or to its critical parameters.

In chapter 3, we provided the theoretical steps leading to the origin of the deterministic reversible terms in the Langevin equation for the three-dimensional isotropic Heisenberg antiferromagnets. To implement the complete dynamics, we devised a novel simulation method that uses a combination of reversible spin precession and relaxation kinetics by alternating between integrating deterministic equations of motion and stochastic Monte Carlo updates over the lattice. We used this hybrid method to characterize the dynamic universality class of three-dimensional isotropic antiferromagnets, model G. We first validated the simulation method by checking the known dynamic exponent $z = 3/2$ for this model. This was achieved by probing the relaxation time of the stationary autocorrelation function that diverges with increasing system size with a power law given by the dynamic exponent. Next, we obtained the aging scaling and the autocorrelation exponent by measuring the two-time spin-spin autocorrelation function of the order parameter following a critical quench. The

asymptotic value of the aging scaling exponent agreed with theoretical prediction. We also verified and recorded the non-universal initial slip exponent which is unique to the class of systems with a non-trivial coupling between a conserved density and a non-conserved order parameter. Using Gaussian distributions of different width as the initial spin configurations, we found that the autocorrelation decay exponent and consequently the initial slip exponent depends on the width of these distributions. Moreover, for sufficiently narrow distributions, the transient oscillations and very slow decay is observed indicating the formation of locally ordered metastable domains that prevents the system from relaxing to its equilibrium.

In chapter 4, we employed the hybrid simulation method to study the critical lines and the bicritical point present in the phase space of three-dimensional anisotropic antiferromagnets in an external field. The dynamic and aging scaling exponents of the model C universality class were obtained from the easy-axis order parameter relaxation. Furthermore, we observed that the conserved density exhibits aging scaling, yet it scales with a negative exponent which is a signature of the system becoming stuck in meta-stable states. Near the model F critical line, the non-vanishing Poisson brackets between the conserved magnetization density and the non-conserved components of the XY-plane staggered magnetization generates propagating spin waves in the ordered phase. Thus aging scaling analysis of the order parameter correlation is not possible. Hence, the dynamic exponent of the model F critical line was determined by analyzing the propagating spin-wave modes in the Fourier space and extracting the characteristic relaxation times. We also verified the dynamic exponent at the bicritical point with existing theoretical predictions and showed that it was indeed different from those of the adjacent critical lines, hence indicating a different universality class at this point.

We hope that the preceding comprehensive characterization of the non-equilibrium aging scaling dynamics in three-dimensional antiferromagnets will aid future theoretical and experimental research in the field of magnetism.

One of the possible extensions of this research is to investigate whether the application of local spatial or temporal control strategies can drive the system from the vicinity one of its critical lines to the other critical line without changing the global parameters. The idea is to essentially utilize the long-range correlations formed near a critical point to drive any local perturbations across the entire system. We are currently performing preliminary studies in this direction by simulating the system near one of the critical lines and then quenching a part of the system with control parameter values of the other critical line. Our early results indicate the spreading of the propagating spin waves from one part of the system to the entire system after

the quench.

The next part of this thesis examines a non-equilibrium model of biological transport phenomena. In chapter 6, we used a variant of the one-dimensional TASEP model to study the internal state-dependent variable step size hopping in a crowded environment of dynein motors. Our data for the average stationary state current in the system indicated the absence of particle-hole symmetry. Next, we investigated the stationary state distributions and observed discrete peaks in the distribution of empty spaces in front of the motors, at gap sizes which are multiples of the maximum step size. Our simulation result was supported by a mean-field analysis of the gap distribution which indicated similar peaks. We also observed interesting damped oscillatory density profiles near the entrance site of the particles for the open boundary case with peaks at sites that are multiples of the maximum step size. We additionally looked at the transient dynamics, specifically the growth of fluctuations or mean square displacement in the system, and found that while for periodic boundary conditions the fluctuations initially grow with superdiffusive power law settling into a diffusive growth later, the open boundary conditions display an initial ballistic growth. Finally, we reported the effects of particle deposition and evaporation randomly from all lattice sites on the stationary state density profile and gap distribution. From a theoretical perspective, we hope that the interesting results that we observe in this study may provide excellent reference points for future studies of transport phenomena and traffic models. It will also be interesting to see whether these results can be reproduced in future in-vitro experiments.

A natural extension of this work is to investigate the motion of the particles on multiple parallel lanes. This can be achieved using an effectively two-dimensional version of the current model. We are currently pursuing this study with the number of lanes the y-direction much lesser than the number of lattice sites in the x-direction, such that we obtain single-file dynamics [114]. Our objective is to obtain a phase diagram by studying the current and the density profiles as a function of various influx and escape rates, various number of lanes, and different attachment and detachment probabilities. Our preliminary results indicate an absence of maximal current phase in this system resulting from the absence of particle-hole symmetry.

Bibliography

[1] E Schrödinger. *What is life?: With mind and matter and autobiographical sketches*. Cambridge University Press, 1992.

[2] V Kampen and N Godfried. *Stochastic processes in physics and chemistry*, volume **1**. Elsevier, 1992.

[3] S-K Ma. *Modern theory of critical phenomena*. Routledge, 2018.

[4] P C Hohenberg and B I Halperin. Theory of dynamic critical phenomena. *Rev. Mod. Phys.*, **49**:435, 1977.

[5] H K Janssen. Dynamical critical phenomena and related topics. *Springer Lecture Notes in Physics*, **104**, 1979.

[6] P M Chaikin, T C Lubensky, and T A Witten. *Principles of condensed matter physics*, volume 10. Cambridge university press Cambridge, 1995.

[7] J Cardy. *Scaling and renormalization in statistical physics*, volume 5. Cambridge university press, 1996.

[8] A N Vasil'ev. *The field theoretic renormalization group in critical behavior theory and stochastic dynamics*. CRC press, 2004.

[9] R Folk and G Moser. Critical dynamics: a field theoretical approach. *J. Phys. A: Math. Gen.*, **39**:R207, 2006.

[10] A Kamenev. *Field theory of non-equilibrium systems*. Cambridge University Press, 2011.

[11] U C Täuber. *Critical dynamics: a field theory approach to equilibrium and non-equilibrium scaling behavior*. Cambridge University Press, 2014.

[12] L D Landau. On the theory of phase transitions. I. *Zh. Eksp. Teor. Fiz.*, **11**:19, 1937.

[13] R K Pathria and P D Beale. *Statistical Mechanics 3rd ed.* Academic Press, Boston, 2011.

[14] B I Halperin and P C Hohenberg. Scaling laws for dynamic critical phenomena. *Phys. Rev.*, **177**:952, 1969.

[15] U C Täuber. Phase transitions and scaling in systems far from equilibrium. *Annu. Rev. Condens. Matter Phys.*, **8**:185–210, 2017.

[16] H K Janssen, B Schaub, and B Schmittmann. New universal short-time scaling behaviour of critical relaxation processes. *Z. Phys. B Condens. Matter*, **73**:539, 1989.

[17] M Henkel and M Pleimling. *Non-Equilibrium Phase Transitions, Volume 2: Ageing and Dynamical Scaling far from Equilibrium (Theoretical and Mathematical Physics)*. Springer, Heidelberg, 2010.

[18] R Nandi and U C Täuber. Nonuniversal critical aging scaling in three-dimensional Heisenberg antiferromagnets. *Phys. Rev. B*, **99**:064417, 2019.

[19] B I Halperin, P C Hohenberg, and S-K Ma. Renormalization-group methods for critical dynamics: II. detailed analysis of the relaxational models. *Phys. Rev. B*, **13**:4119, 1976.

[20] J D Gunton and K Kawasaki. Renormalization group equations in critical dynamics. II: Binary liquid, superfluid helium and magnets. *Prog. Theor. Phys.*, **56**:61, 1976.

[21] R Freedman and G F Mazenko. Critical dynamics of isotropic antiferromagnets using renormalization-group methods: $T \geq T_N$. *Phys. Rev. B*, **13**:4967, 1976.

[22] L Sasvári, F Schwabl, and P Szépfalusy. Hydrodynamics of an n-component phonon system. *Physica A*, **81**:108, 1975.

[23] L Sasvári and P Szépfalusy. Critical dynamics of a stochastic n-vector model below T_c. *Physica A: Statistical Mechanics and its Applications*, **90**:626, 1978.

[24] C De Dominicis and L Peliti. Field-theory renormalization and critical dynamics above T_c: Helium, antiferromagnets, and liquid-gas systems. *Phys. Rev. B*, **18**:353, 1978.

[25] D P Landau and M Krech. Spin dynamics simulations of classical ferro-and antiferromagnetic model systems: comparison with theory and experiment. *J. Phys. Condens. Matter*, **11**:R179, 1999.

[26] K Chen and D P Landau. Spin-dynamics study of the dynamic critical behavior of the three-dimensional classical Heisenberg ferromagnet. *Phys. Rev. B*, **49**:3266, 1994.

[27] G Gyorgyi, I Kondor, L Sasvari, and T Tel. *From Phase Transitions to Chaos: Topics in Modern Statistical Physics*. World Scientific, 1992.

[28] P Calabrese and A Gambassi. Ageing properties of critical systems. *J. Phys. A: Math. Gen.*, **38**:R133, 2005.

[29] C Sire. Autocorrelation exponent of conserved spin systems in the scaling regime following a critical quench. *Phys. Rev. Lett.*, **93**:130602, 2004.

[30] K Oerding and H K Janssen. Non-equilibrium critical relaxation with reversible mode coupling. *J. Phys. A: Math. Gen.*, **26**:5295, 1993.

[31] J Zinn-Justin. Precise determination of critical exponents and equation of state by field theory methods. *Phys. Rep.*, **344**:159, 2001. Renormalization group theory in the new millennium.

[32] P Peczak, A M Ferrenberg, and D P Landau. High-accuracy monte carlo study of the three-dimensional classical Heisenberg ferromagnet. *Phys. Rev. B*, **43**:6087, 1991.

[33] K Chen, A M Ferrenberg, and D P Landau. Static critical behavior of three-dimensional classical Heisenberg models: A high-resolution monte carlo study. *Phys. Rev. B*, **48**:3249, 1993.

[34] C Holm and W Janke. Critical exponents of the classical three-dimensional Heisenberg model: A single-cluster monte carlo study. *Phys. Rev. B*, **48**:936, 1993.

[35] F Schwabl and K H Michel. Hydrodynamics of Heisenberg ferromagnets. *Phys. Rev. B*, **2**:189, 1970.

[36] C M V Vliet. *Equilibrium and Non-Equilibrium Statistical Mechanics:(New and Revised Printing)*. World Scientific Publishing Company, 2008.

[37] S-K Ma and G F Mazenko. Critical dynamics of ferromagnets in 6- ε dimensions. *Phys. Rev. Lett.*, **33**:1383, 1974.

[38] K Kawasaki. Diffusion constants near the critical point for time-dependent ising models. I. *Phys. Rev.*, **145**:224, 1966.

[39] A K Murtazaev, V A Mutailamov, I K Kamilov, K S Khizriev, and Y K Abuev. Investigation on the critical dynamics of real magnetics models by computational physics methods. *J. Magn. Magn. Mater.*, **258**:48, 2003.

[40] A Bunker, K Chen, and D P Landau. Critical dynamics of the body-centered-cubic classical Heisenberg antiferromagnet. *Phys. Rev. B*, **54**:9259, 1996.

[41] S-H Tsai and D P Landau. Critical dynamics of the simple-cubic Heisenberg antiferromagnet $RbMnF_3$: Extrapolation to q= 0. *Phys. Rev. B*, **67**:104411, 2003.

[42] R Abe. Dynamics of the ising model near the transition point. *Progress of Theoretical Physics*, **39**:947, 1968.

[43] D P Landau and K Binder. Phase diagrams and multicritical behavior of a three-dimensional anisotropic Heisenberg antiferromagnet. *Phys. Rev. B*, **17**:2328, 1978.

[44] Riya Nandi and Uwe C Täuber. Critical dynamics of anisotropic antiferromagnets in an external field. *Physical Review E*, 102(5):052114, 2020.

[45] J M Kosterlitz, D R Nelson, and M E Fisher. Bicritical and tetracritical points in anisotropic antiferromagnetic systems. *Phys. Rev. B*, **13**:412, 1976.

[46] K-S Liu and M E Fisher. Quantum lattice gas and the existence of a supersolid. *J. Low Temp. Phys.*, **10**:655, 1973.

[47] Y Shapira and S Foner. Magnetic phase diagram of MnF_2 from ultrasonic and differential magnetization measurements. *Phys. Rev. B*, **1**:3083, 1970.

[48] H Rohrer and Ch Gerber. Bicritical and tetracritical behavior of $GdAlO_3$. *Phys. Rev. Lett.*, **38**:909, 1977.

[49] N F Oliveira Jr, A F Paduan Filho, S R Salinas, and C C Becerra. Magnetic phase diagram of $NiCl_2 \cdot 6H_2O$: The low-temperature canted-paramagnetic boundary and the bicritical point. *Phys. Rev. B*, **18**:6165, 1978.

[50] M E Fisher and D R Nelson. Spin flop, supersolids, and bicritical and tetracritical points. *Phys. Rev. Lett.*, **32**:1350, 1974.

[51] O G Mouritsen, E K Hansen, and S J K Jensen. General correlation function series: Phase diagram of the anisotropic Heisenberg antiferromagnet in a field. *Phys. Rev. B*, **22**:3256, 1980.

[52] R Folk, Y Holovatch, and G Moser. Field theory of bicritical and tetracritical points. I. statics. *Phys. Rev. E*, **78**:041124, 2008.

[53] R Folk, Y Holovatch, and G Moser. Field theory of bicritical and tetracritical points. II. relaxational dynamics. *Phys. Rev. E*, **78**:041125, 2008.

[54] R Folk, Y Holovatch, and G Moser. Field theory of bicritical and tetracritical points. III. relaxational dynamics including conservation of magnetization (model c). *Phys. Rev. E*, **79**:031109, 2009.

[55] R Folk, Y Holovatch, and G Moser. Field theory of bicritical and tetracritical points. IV. critical dynamics including reversible terms. *Phys. Rev. E*, **85**:021143, 2012.

[56] P Calabrese, A Pelissetto, and E Vicari. Multicritical behavior of $O(n_1) \bigoplus O(n_2)$-symmetric systems. *Phys. Rev. B*, **67**:054505, 2003.

[57] W Selke. Evidence for a bicritical point in the xxz Heisenberg antiferromagnet on a simple cubic lattice. *Phys. Rev. E*, **83**:042102, 2011.

[58] S-H Tsai, S Hu, and D P Landau. Bicritical or tetracritical: the 3d anisotropic Heisenberg antiferromagnet. *J. Phys.: Conf. Ser.*, **487**:012005, 2014.

[59] R J Glauber. Time-dependent statistics of the ising model. *J. Math. Phys.*, **4**:294, 1963.

[60] V K Akkineni and U C Täuber. Nonequilibrium critical dynamics of the relaxational models c and d. *Phys. Rev. E*, **69**:036113, 2004.

[61] R Folk and G Moser. Critical dynamics of stochastic models with energy conservation (model C). *Phys. Rev. E*, **69**:036101, 2004.

[62] M Campostrini, M Hasenbusch, A Pelissetto, P Rossi, and E Vicari. Critical exponents and equation of state of the three-dimensional Heisenberg universality class. *Phys. Rev. B*, **65**:144520, 2002.

[63] D P Landau. Computer simulation studies of critical phenomena. *Physica A*, **205**:41, 1994.

[64] K Oerding and H K Janssen. Nonequilibrium critical relaxation with coupling to a conserved density. *J. Phys. A: Math. Gen.*, **26**:3369, 1993.

[65] W Koch and V Dohm. Finite-size effects on critical diffusion and relaxation towards metastable equilibrium. *Phys. Rev. E*, **58**:R1179, 1998.

[66] C Godrèche, F Krzakała, and F Ricci-Tersenghi. Non-equilibrium critical dynamics of the ferromagnetic ising model with kawasaki dynamics. *J. Stat. Mech.*, **2004**:P04007, 2004.

[67] B D Josephson. Relation between the superfluid density and order parameter for superfluid he near tc. *Phys. Lett.*, **21**:608, 1966.

[68] B I Halperin and P C Hohenberg. Hydrodynamic theory of spin waves. *Phys. Rev.*, **188**:898, 1969.

[69] S Chen and U C Täuber. Non-equilibrium relaxation in a stochastic lattice lotka–volterra model. *Phys. Biol.*, **13**:025005, 2016.

[70] C T MacDonald, J H Gibbs, and Pipkin A C. Kinetics of biopolymerization on nucleic acid templates. *Biopolymers*, **6**:1, 1968.

[71] F. Spitzer. Interacting markov processes. *Adv. Math.*, **5**:246, 1970.

[72] M Schliwa. *Molecular motors*. Wiley online Library,New York, 2004.

[73] J Howard. *Mechanics of Motor Proteins and the Cytoskeleton*. Sinauer Associates,Sunderland, MA, 2001.

[74] A B Kolomeisky. *Motor proteins and molecular motors*. CRC press, 2015.

[75] M Schliwa and G Woehlke. Molecular motors. *Nature*, **422**:759, 2003.

[76] G Bhabha, G T Johnson, C M Schroeder, and R D Vale. How dynein moves along microtubules. *Trends Biochem. Sci.*, **41**:94, 2016. Special Issue: 40 Years of TiBS.

[77] R Mallik, B C Carter, S A Lex, S J King, and S P Gross. Cytoplasmic dynein functions as a gear in response to load. *Nature*, **427**:649, 2004.

[78] M E Fisher and A B Kolomeisky. The force exerted by a molecular motor. *Proc. Natl. Acad. Sci.*, **96**:6597, 1999.

[79] T Chou, K Mallick, and R K P Zia. Non-equilibrium statistical mechanics: from a paradigmatic model to biological transport. *Rep. Prog. Phys*, **74**:116601, 2011.

[80] F Jülicher, A Ajdari, and J Prost. Modeling molecular motors. *Rev. Mod. Phys.*, **69**:1269, 1997.

[81] H Wang and G Oster. Ratchets, power strokes, and molecular motors. *Appl. Phys. A*, **75**:315, 2002.

[82] A Kunwar, A Schadschneider, and D Chowdhury. From aggressive driving to molecular motor traffic. *J. Phys. A: Math. Gen.*, **39**:14263, 2006.

[83] S Mukherji. Model for the unidirectional motion of a dynein molecule. *Phys. Rev. E*, **77**:051916, 2008.

[84] M P Singh, R Mallik, S P Gross, and C Y Clare. Monte carlo modeling of single-molecule cytoplasmic dynein. *Proc. Natl. Acad. Sci.*, 102(34):12059, 2005.

[85] P Ashwin, C Lin, and G Steinberg. Queueing induced by bidirectional motor motion near the end of a microtubule. *Phys. Rev. E*, **82**:051907, 2010.

[86] A K Rai, A Rai, A J Ramaiya, R Jha, and R Mallik. Molecular adaptations allow dynein to generate large collective forces inside cells. *Cell*, **152**:172, 2013.

[87] K Visscher, M J Schnitzer, and S M Block. Single kinesin molecules studied with a molecular force clamp. *Nature*, **400**:184, 1999.

[88] C M Coppin, Daniel W Pierce, L Hsu, and R D Vale. The load dependence of kinesin's mechanical cycle. *Proc. Natl. Acad. Sci.*, **94**:8539, 1997.

[89] A Parmeggiani, T Franosch, and E Frey. Totally asymmetric simple exclusion process with langmuir kinetics. *Phys. Rev. E*, **70**:046101, 2004.

[90] A Kunwar, S K Tripathy, J Xu, M K Mattson, P Anand, R Sigua, M Vershinin, R J McKenney, C Y Clare, A Mogilner, et al. Mechanical stochastic tug-of-war models cannot explain bidirectional lipid-droplet transport. *Proc. Natl. Acad. Sci.*, **108**:18960, 2011.

[91] M A DeWitt, A Y Chang, P A Combs, and A Yildiz. Cytoplasmic dynein moves through uncoordinated stepping of the AAA+ ring domains. *Science*, **335**:221, 2012.

[92] W Qiu, N D Derr, B S Goodman, E Villa, D Wu, W Shih, and S L Reck-Peterson. Dynein achieves processive motion using both stochastic and coordinated stepping. *Nat. Struct. Mol. Bio.*, **19**:193, 2012.

[93] K Shibata, M Miura, Y Watanabe, K Saito, A Nishimura, K Furuta, and Y Y Toyoshima. A single protofilament is sufficient to support unidirectional walking of dynein and kinesin. *PLOS ONE*, **7**:1, 2012.

[94] S L Reck-Peterson and R D Vale. Molecular dissection of the roles of nucleotide binding and hydrolysis in dynein's AAA domains in saccharomyces cerevisiae. *Proc. Natl. Acad. Sci.*, **101**:1491, 2004.

[95] T Kon, M Nishiura, R Ohkura, Y Y Toyoshima, and K Sutoh. Distinct functions of nucleotide-binding/hydrolysis sites in the four AAA modules of cytoplasmic dynein. *Biochem.*, **43**:11266, 2004.

[96] C Godrèche and J-M Drouffe. Coarsening dynamics of zero-range processes. *J. Phys. A: Math. Theor.*, **50**:015005, nov 2016.

[97] G P Shrivastav, V Banerjee, and S Puri. Mass-transport models with multiple-chipping processes. *Eur. Phys. J. B*, **78**:217, 2010.

[98] S Gupta, S N Majumdar, C Godrèche, and M Barma. Tagged particle correlations in the asymmetric simple exclusion process: Finite-size effects. *Phys. Rev. E*, **76**:021112, 2007.

[99] Priyanka and K Jain. Critical dynamics of the jamming transition in one-dimensional nonequilibrium lattice-gas models. *Phys. Rev. E*, **93**:042104, 2016.

[100] L Bruno, V Levi, M Brunstein, and M A Desposito. Transition to superdiffusive behavior in intracellular actin-based transport mediated by molecular motors. *Phys. Rev. E*, **80**:011912, 2009.

[101] A W C Lau, B D Hoffman, A Davies, J C Crocker, and T C Lubensky. Microrheology, stress fluctuations, and active behavior of living cells. *Phys. Rev. Lett.*, **91**:198101, 2003.

[102] P Bursac, G Lenormand, B Fabry, M Oliver, D A Weitz, V Viasnoff, J P Butler, and J J Fredberg. Cytoskeletal remodelling and slow dynamics in the living cell. *Nat. Mater.*, **4**:557, 2005.

[103] S Sharma and P Biswas. Unusual dynamics of hydration water around motor proteins with long-ranged hydrodynamic fluctuations. *Physica A*, 534:122045, 2019.

[104] A Caspi, R Granek, and M Elbaum. Enhanced diffusion in active intracellular transport. *Phys. Rev. Lett*, **85**:5655, 2000.

[105] G M Schütz. Exactly solvable models for many-body systems far from equilibrium. *Phase transitions and critical phenomena*, 2000.

[106] R Huang, I Chavez, K M Taute, B Lukić, S Jeney, M G. Raizen, and E-L Florin. Direct observation of the full transition from ballistic to diffusive brownian motion in a liquid. *Nat. Phys.*, **7**:576, 2011.

[107] M Galanti, D Fanelli, and F Piazza. Persistent random walk with exclusion. *Eur. Phys. J. B*, **86**:456, 2013.

[108] A Parmeggiani, F Jülicher, L Peliti, and J Prost. Detachment of molecular motors under tangential loading. *EPL*, **56**:603, 2001.

[109] Y Kafri, D K Lubensky, and D R Nelson. Dynamics of molecular motors with finite processivity on heterogeneous tracks. *Phys. Rev. E*, **71**:041906, 2005.

[110] K G Ohashi, L Han, B Mentley, J Wang, J Fricks, and W O Hancock. Load-dependent detachment kinetics plays a key role in bidirectional cargo transport by kinesin and dynein. *Traffic*, **20**:284, 2019.

[111] A R Rogers, J W Driver, P E Constantinou, D K Jamison, and M R Diehl. Negative interference dominates collective transport of kinesin motors in the absence of load. *Phys. Chem. Chem. Phys.*, **11**:4882, 2009.

[112] K Furuta, A Furuta, Y Y Toyoshima, M Amino, K Oiwa, and H Kojima. Measuring collective transport by defined numbers of processive and nonprocessive kinesin motors. *Proc. Natl. Acad. Sci.*, **110**:501, 2013.

[113] N D Derr, B S Goodman, R Jungmann, A E Leschziner, W M Shih, and S L Reck-Peterson. Tug-of-war in motor protein ensembles revealed with a programmable dna origami scaffold. *Science*, **338**:662, 2012.

[114] PL Krapivsky, Kirone Mallick, and Tridib Sadhu. Dynamical properties of single-file diffusion. *Journal of Statistical Mechanics: Theory and Experiment*, 2015(9):P09007, 2015.